Fluctuation-exchange theory for general lattice Hamiltonians

Gökhan Esirgen and N. E. Bickers
Department of Physics, University of Southern California, Los Angeles, California 90089
(Received 21 August 1996)

The fluctuation-exchange, or FLEX, approximation for interacting electrons is derived for lattice Hamiltonians with general instantaneous one- and two-body terms. The use of a two-body basis set indexed by relative separation, rather than relative momentum, is emphasized. The fluctuation-exchange approximation for the three-orbital CuO_2 model with on-site and near-neighbor Coulomb interactions is solved for one-particle properties. Unit-cell densities corresponding to both ''hole doping'' and ''electron doping'' are studied. The model is found to be far from a charge-density instability for all reasonable parameter values. The only nearly unstable particle-hole channel for unit-cell densities close to unity has $\mathbf{Q}\sim(\pi,\pi)$ and $S=1$ (antiferromagnetic). The Fermi surface of the interacting system is computed, and the Luttinger theorem verified numerically in its most general context. Orbital-projected occupancy factors and spectral densities are examined. [S0163-1829(96)07148-2]

I. INTRODUCTION

In recent years, self-consistent-field (SCF) approximations[1] have been used to study tight-binding models for correlated electrons. Previous work has been limited to the simplest electronic orbital and interaction structures (viz., the one-orbital Hubbard model[2–10] and a trivial extension[11]). In this paper we extend the SCF analysis to general tight-binding models and perform calculations of one-particle correlation functions for the three-orbital model[12] most commonly used to describe the high-temperature cuprate superconductors.

We begin by briefly reprising the motivation behind the SCF approach. In any SCF approximation the effect of two-particle interactions is partially eliminated by the introduction of a self-consistently determined one-particle potential. At Hartree-Fock level (see Fig. 1) the one-particle potential is instantaneous, and the system may be described in terms of a modified Hamiltonian. In approximations beyond Hartree-Fock, the potential becomes time-dependent, and the system must be described in terms of an action functional.

A conceptually appealing approach for systems in which particle-hole or particle-particle pair fluctuations are large is the so-called fluctuation-exchange, or FLEX, approximation.[1,13] This approach takes the view that one-particle excitations interact through the exchange of pair fluctuations. (This view can, in principle, be made exact by introducing appropriate two-particle-irreducible vertex functions.) If correlations between elements of the pair fluctuation are ignored, the simplest ''correlation'' contributions to the one-particle SCF are generated (see Fig. 2). Note that the uncorrelated pair fluctuation propagator is just a convolution of two one-particle propagators. The simplest approximation which correlates the elements of the pair using an irreducible vertex function (in contrast with perturbation theory) is FLEX. In this case the irreducible vertex function is just the unrenormalized two-particle interaction.

The FLEX approximation provides a simple enlargement of Hartree-Fock theory with many of the features familiar from the Migdal-Eliashberg treatment[14,15] of electron-phonon interactions. The quantitative accuracy of the approximation may be improved by replacing the unrenormalized interaction in the pair fluctuation propagators with a self-consistent vertex function, or pseudopotential.[3,16] The pseudopotential may be determined by solving a set of parquet equations.

As mentioned above, previous FLEX studies have been limited to the simplest tight-binding models. In Sec. II below we derive the most general form of the FLEX approximation for Bravais lattices with an orbital basis and an arbitrary instantaneous two-particle interaction. This extension allows

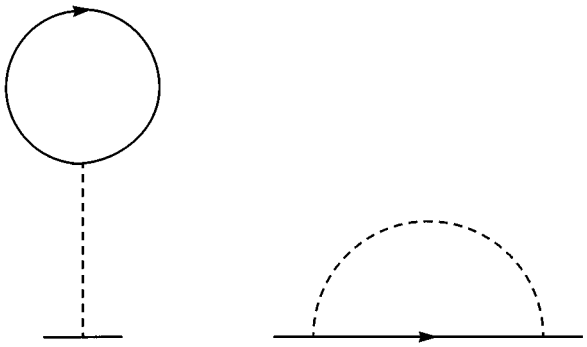

FIG. 1. Hartree (direct) and Fock (exchange) SCF diagrams. Solid lines represent one-particle propagators, and dashed lines the two-body interaction.

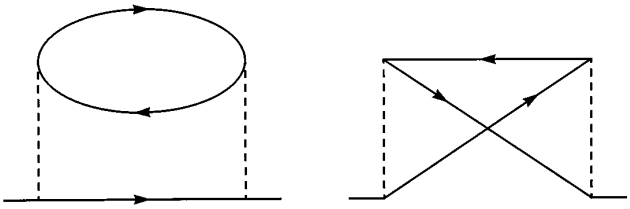

FIG. 2. Simplest correlation contributions to the one-particle SCF.

the incorporation of increasingly realistic features. Such features must be included if the eventual goal is a predictive capability for real materials. The crucial technical feature which makes solution of such approximations feasible is the introduction of a new basis set[17–21] for pair fluctuation propagators. In Sec. III we discuss a number of technical points associated with solution of the FLEX equations for multiorbital systems.

In parallel with development of the general formalism, we specialize our analysis to the now standard three-orbital model for CuO_2 layers in the cuprate superconductors. In Sec. IV we present and discuss results for one-particle correlation functions in this model, using a canonical parameter set derived from density-functional studies and a variety of other parameter choices. We summarize our analysis in Sec. V, and briefly discuss the next phase of this calculational program, the analysis of two-particle instabilities in the CuO_2 model, and more general systems.

II. TECHNIQUE FOR GENERAL COULOMB INTERACTIONS

In this section we develop the form of the FLEX approximation for a general instantaneous local interaction in a tight-binding model for a Bravais lattice with a basis. (This development may be extended to time-dependent interactions in a natural way.[1])

Assume that the Bravais lattice consists of N unit cells with periodic boundary conditions, and that each unit cell contains a set of orthonormal orbitals ϕ_a. Assume in addition that orbitals in different unit cells are also orthogonal. If the one-particle Schrödinger operator (electronic kinetic energy+Coulomb interaction with the lattice) is written $h^0(\mathbf{r})$, the second-quantized one-particle Hamiltonian takes the form

$$\hat{H}_0=\sum_{\sigma}\sum_{ab}\sum_{\mathbf{R}_a\mathbf{R}_b} h^0_{ab}(\mathbf{R}_a,\mathbf{R}_b)c^{\dagger}_{a\sigma}(\mathbf{R}_a)c_{b\sigma}(\mathbf{R}_b), \tag{1}$$

where

$$h^0_{ab}(\mathbf{R}_a,\mathbf{R}_b)=\int d\mathbf{r}\ \phi^*_a(\mathbf{r}-\mathbf{R}_a)h^0(\mathbf{r})\phi_b(\mathbf{r}-\mathbf{R}_b). \tag{2}$$

In these equations $\mathbf{R}_a$ is the origin of the unit cell containing orbital a. Since the system is periodic, $h^0_{ab}(\mathbf{R}_a,\mathbf{R}_b)$ depends only on the relative separation

$$\Delta\mathbf{R}_{ab}=\mathbf{R}_a-\mathbf{R}_b\,. \tag{3}$$

It is convenient to Fourier transform using

$$c^{\dagger}_{a\sigma}(\mathbf{R}_a)=\frac{1}{\sqrt{N}}\sum_{\mathbf{k}} e^{-i\mathbf{k}\cdot\mathbf{R}_a}c^{\dagger}_{a\sigma}(\mathbf{k}). \tag{4}$$

Thus

$$\hat{H}_0=\sum_{\sigma}\sum_{ab}\sum_{\mathbf{k}} h^0_{ab}(\mathbf{k})c^{\dagger}_{a\sigma}(\mathbf{k})c_{b\sigma}(\mathbf{k}), \tag{5}$$

with

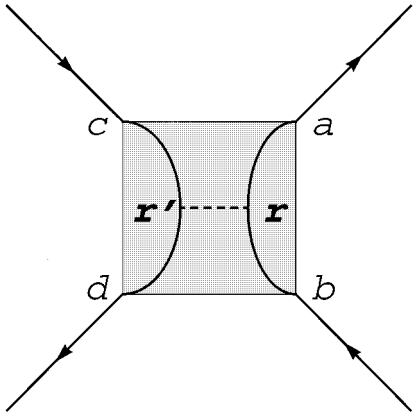

FIG. 3. Direct interaction vertex $V^{\rm dir}_{ab,cd}(\mathbf{R}_a\mathbf{R}_b,\mathbf{R}_c\mathbf{R}_d)$. The positions $\mathbf{r}$ and $\mathbf{r}'$ are integration variables.

$$h^0_{ab}(\mathbf{k})=\sum_{\Delta\mathbf{R}_{ab}} e^{-i\mathbf{k}\cdot\Delta\mathbf{R}_{ab}}h^0_{ab}(\Delta\mathbf{R}_{ab}). \tag{6}$$

This last form is convenient for SCF calculations. Note that the quantity $h^0_{ab}(\mathbf{k})$ may be treated as the (a,b) element of matrix $h^0(\mathbf{k})$, defined with indices in orbital space. The eigenvalues of h^0 are just the one-particle band energies.

It is next necessary to develop a notation and formalism for the two-particle interaction $v(\mathbf{r}-\mathbf{r}')$. The second-quantized interaction may be written in two equivalent forms related by a ''crossing symmetry.'' The use of these two forms simplifies notation for the FLEX SCF and vertex functions. The ''direct'' interaction connects particle-hole states in which the final and initial pairs are created at points $\mathbf{r}$ and $\mathbf{r}'$, respectively (see Fig. 3):

$$\begin{aligned}\hat{V}&=\tfrac{1}{2}\sum_{\sigma\sigma'}\int d\mathbf{r}\int d\mathbf{r}'\,v(\mathbf{r}-\mathbf{r}'):\psi^{\dagger}_{\sigma}(\mathbf{r})\psi_{\sigma}(\mathbf{r})\psi^{\dagger}_{\sigma'}(\mathbf{r}')\psi_{\sigma'}(\mathbf{r}'):\\&=\tfrac{1}{2}\sum_{\sigma\sigma'}\sum_{ab,cd}\sum_{\mathbf{R}_a\mathbf{R}_b,\mathbf{R}_c\mathbf{R}_d} V^{\rm dir}_{ab,cd}(\mathbf{R}_a\mathbf{R}_b,\mathbf{R}_c\mathbf{R}_d)\\&\quad\times:c^{\dagger}_{a\sigma}(\mathbf{R}_a)c_{b\sigma}(\mathbf{R}_b)c^{\dagger}_{d\sigma'}(\mathbf{R}_d)c_{c\sigma'}(\mathbf{R}_c):\end{aligned} \tag{7}$$

with

$$\begin{aligned}V^{\rm dir}_{ab,cd}(\mathbf{R}_a\mathbf{R}_b,\mathbf{R}_c\mathbf{R}_d)=\int d\mathbf{r}\int d\mathbf{r}'\,\phi^*_a(\mathbf{r}-\mathbf{R}_a)\phi_b(\mathbf{r}-\mathbf{R}_b)\\\times v(\mathbf{r}-\mathbf{r}')\phi^*_d(\mathbf{r}'-\mathbf{R}_d)\phi_c(\mathbf{r}'-\mathbf{R}_c).\end{aligned} \tag{8}$$

In the subscript for $V^{\rm dir}$, ab is a compound index indicating a particle-hole pair in orbitals a and b; likewise for subscript cd. The colons indicate normal-ordering of the operator product.

By translational invariance the Coulomb integral $V^{\rm dir}$ depends on only three intercell displacements (see Fig. 4). It is convenient to adopt a notation which emphasizes this feature by writing

$$V^{\rm dir}_{ab,cd}(\mathbf{R}_a\mathbf{R}_b,\mathbf{R}_c\mathbf{R}_d)\equiv V^{\rm dir}_{ab,cd}(\Delta\mathbf{R}_{ac};\Delta\mathbf{R}_{ab},\Delta\mathbf{R}_{cd}), \tag{9a}$$

where, for example,

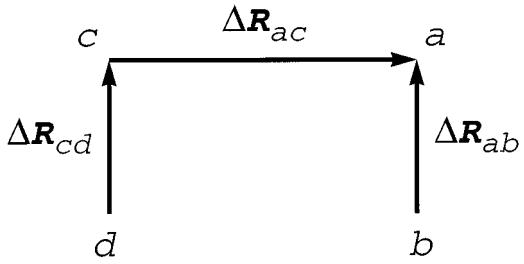

FIG. 4. Definition of the relative displacement variables $\Delta\mathbf{R}$.

$$\Delta\mathbf{R}_{ac}\equiv\mathbf{R}_a-\mathbf{R}_c\,. \tag{9b}$$

The first argument of $V^{\rm dir}$ on the right-hand side is the displacement from the particle in the initial state to the particle in the final state. The second and third arguments are the displacements from the hole to the particle in the final and initial states, respectively.

The expression in Eq. (8) is more general than the Coulomb interaction used in most studies of tight-binding models. It is conventional to restrict attention to terms in which $\Delta\mathbf{R}_{ab}$ and $\Delta\mathbf{R}_{cd}$ are both zero. This restriction is sensible since the orbitals $\phi_a(\mathbf{r}-\mathbf{R}_a)$ are assumed to fall off exponentially: the products $\phi_a^*(\mathbf{r}-\mathbf{R}_a)\phi_b(\mathbf{r}-\mathbf{R}_b)$ are small everywhere unless $\mathbf{R}_a=\mathbf{R}_b$. Furthermore, the largest contributions to $V^{\rm dir}$ arise from combinations with $a=b$ and $c=d$. Combinations which correspond to particle-hole pairs in different orbitals ($a\neq b$ or $c\neq d$) are also allowed, but are generally small by orthogonality arguments. Note that these latter combinations include the exchange integrals J which arise in atomic theory.

As a concrete example, consider the three-orbital CuO_2 model with short-range Coulomb integrals mentioned in the Introduction. The orbital labels in this case range over $a=d$, $p_x\equiv x$, and $p_y\equiv y$. The unit cell is indicated in Fig. 5. The nonzero Coulomb integrals retained are

$$U_{dd}=V^{\rm dir}_{dd,dd}(0;0,0),$$

$$U_{pp}=V^{\rm dir}_{xx,xx}(0;0,0)=V^{\rm dir}_{yy,yy}(0;0,0), \tag{10}$$

$$\begin{aligned}U_{pd}&=V^{\rm dir}_{dd,xx}(0;0,0)=V^{\rm dir}_{dd,xx}(+\hat{x};0,0)=V^{\rm dir}_{xx,dd}(0;0,0)\\&=V^{\rm dir}_{xx,dd}(-\hat{x};0,0)=V^{\rm dir}_{dd,yy}(0;0,0)=V^{\rm dir}_{dd,yy}(+\hat{y};0,0)\\&=V^{\rm dir}_{yy,dd}(0;0,0)=V^{\rm dir}_{yy,dd}(-\hat{y};0,0).\end{aligned}$$

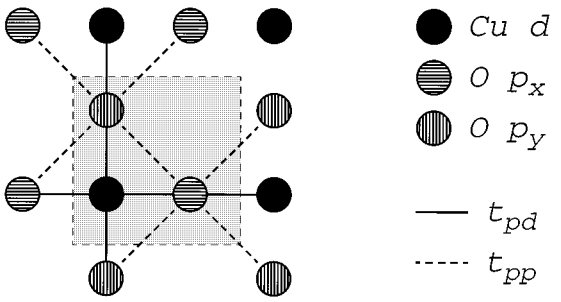

FIG. 5. Unit cell for the three-orbital CuO_2 model. The one-body transfer integrals t_{pd} and t_{pp} are indicated.

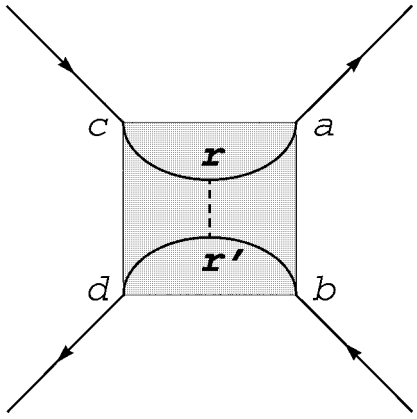

FIG. 6. Exchange interaction vertex $V^{\rm exc}_{ab,cd}(\Delta\mathbf{R}_{ac};\Delta\mathbf{R}_{ab},\Delta\mathbf{R}_{cd})$.

Using a crossing operation to flip the ''b'' and ''c'' legs in Fig. 3, the general interaction may be rewritten in an ''exchange'' form (see Fig. 6):

$$\begin{aligned}\hat{V}=-\tfrac{1}{2}\sum_{\sigma\sigma'}\sum_{ab,cd}\sum_{\mathbf{R}_a\mathbf{R}_b,\mathbf{R}_c\mathbf{R}_d}&V^{\rm exc}_{ab,cd}(\Delta\mathbf{R}_{ac};\Delta\mathbf{R}_{ab},\Delta\mathbf{R}_{cd})\\&\times{:}c^\dagger_{a\sigma}(\mathbf{R}_a)c_{b\sigma'}(\mathbf{R}_b)c^\dagger_{d\sigma'}(\mathbf{R}_d)c_{c\sigma}(\mathbf{R}_c){:}\end{aligned} \tag{11}$$

with

$$\begin{aligned}&V^{\rm exc}_{ab,cd}(\Delta\mathbf{R}_{ac};\Delta\mathbf{R}_{ab},\Delta\mathbf{R}_{cd})\\&\quad=\int d\mathbf{r}\int d\mathbf{r}'\,\phi_a^*(\mathbf{r})\phi_c(\mathbf{r}+\Delta\mathbf{R}_{ac})v(\mathbf{r}-\mathbf{r}')\\&\qquad\times\phi_d^*(\mathbf{r}'+\Delta\mathbf{R}_{ac}+\Delta\mathbf{R}_{cd})\phi_b(\mathbf{r}'+\Delta\mathbf{R}_{ab}).\end{aligned} \tag{12}$$

Note that this is simply a notational change, not a new interaction. The Coulomb integrals $V^{\rm dir}$ and $V^{\rm exc}$ obey the crossing symmetry relation

$$V^{\rm dir}_{ab,cd}(\Delta\mathbf{R}_{ac};\Delta\mathbf{R}_{ab},\Delta\mathbf{R}_{cd})=V^{\rm exc}_{ac,bd}(\Delta\mathbf{R}_{ab};\Delta\mathbf{R}_{ac},\Delta\mathbf{R}_{bd}). \tag{13}$$

The minus sign in Eq. (11) arises from the reordering of fermion destruction operators. (The exchange form of the general interaction should not be confused with the exchange integrals mentioned above, which appear in both $V^{\rm dir}$ and $V^{\rm exc}$.)

The FLEX approximation for interaction $\hat{V}$ can be generated using the formalism of Ref. 1 in a number of ways. For maximum efficiency it is essential to label the fluctuation propagators using total pair momentum $\mathbf{Q}$ and frequency $i\Omega$ (exploiting translational invariance in space and time); and relative displacement coordinates $\Delta\mathbf{R}$ and $\Delta\tau$ (exploiting the short-range, instantaneous character of $\hat{V}$).

We begin by defining Coulomb integrals Fourier-transformed on the displacement variable $\Delta\mathbf{R}_{ac}$:

$$\begin{aligned}V^{\rm dir}_{ab,cd}(\mathbf{Q};\Delta\mathbf{R}_{ab},\Delta\mathbf{R}_{cd})=\sum_{\Delta\mathbf{R}_{ac}}&e^{-i\mathbf{Q}\cdot\Delta\mathbf{R}_{ac}}\\&\times V^{\rm dir}_{ab,cd}(\Delta\mathbf{R}_{ac};\Delta\mathbf{R}_{ab},\Delta\mathbf{R}_{cd}),\end{aligned} \tag{14}$$

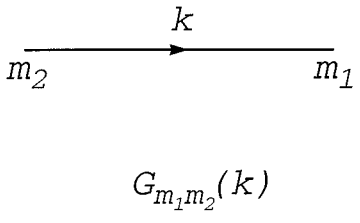

FIG. 7. One-particle propagator $G_{m_1 m_2}(k)$.

and likewise for $V^{\rm exc}$. In order to calculate $\Sigma(k,\sigma)$ it is useful to have the interaction $\hat{V}$ written out in terms of Fourier-transformed fermion operators. Invoking Eq. (4) one obtains

$$\hat{V}=\tfrac{1}{2}\sum_{\sigma\sigma'}\sum_{ab,cd}\sum_{\Delta\mathbf{R}_{ab},\Delta\mathbf{R}_{cd}}\frac{1}{N}\sum_{\mathbf{k}\mathbf{k}'\mathbf{Q}} e^{-i\mathbf{k}\cdot\Delta\mathbf{R}_{ab}}e^{i\mathbf{k}'\cdot\Delta\mathbf{R}_{cd}} \times V^{\rm dir}_{ab,cd}(\mathbf{Q};\Delta\mathbf{R}_{ab},\Delta\mathbf{R}_{cd}) \times :c^{\dagger}_{a\sigma}(\mathbf{k}+\mathbf{Q})c_{b\sigma}(\mathbf{k})c^{\dagger}_{d\sigma'}(\mathbf{k}')c_{c\sigma'}(\mathbf{k}'+\mathbf{Q}):, \quad (15)$$

and an analogous expression in terms of $V^{\rm exc}$. While the sums on $\Delta\mathbf{R}_{ab}$ and $\Delta\mathbf{R}_{cd}$ could be performed at this stage [compare Eq. (6)], it is important to retain the phase factors explicitly.

Expressions for the FLEX SCF may now be written down in a computationally tractable form. We employ the notation of Ref. 1, writing the one-particle SCF Σ and propagator G as matrices in orbital space (see Fig. 7). The combined momentum-frequency variable $(\mathbf{k},i\omega)$ is abbreviated k. The propagator and SCF are connected by the relation

$$G(k,\sigma)=\{i\omega-[h_0(\mathbf{k})-\mu]-\Sigma(k,\sigma)\}^{-1}, \quad (16)$$

with h_0 the matrix introduced in Eq. (6). Note that the propagator defined in this way has units of inverse energy (and differs by a factor of T from the definition in Ref. 1).

The Hartree contribution to the SCF (Fig. 8) takes the form

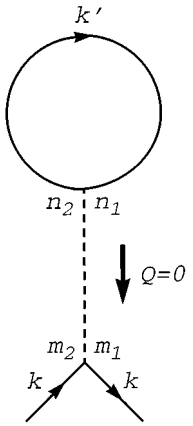

FIG. 8. Hartree contribution $\Sigma^{(1H)}_{m_1 m_2}(k)$ to the one-particle SCF.

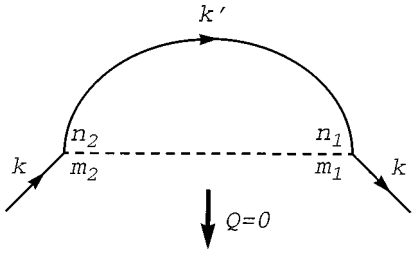

FIG. 9. Fock contribution $\Sigma^{(1F)}_{m_1 m_2}(k)$ to the one-particle SCF.

$$\Sigma^{(1H)}_{m_1 m_2}(k)=\frac{T}{N}\sum_{n_1 n_2}\sum_{\Delta\mathbf{R}_{m_1 m_2},\Delta\mathbf{R}_{n_1 n_2}} e^{-i\mathbf{k}\cdot\Delta\mathbf{R}_{m_1 m_2}} \times 2V^{\rm dir}_{m_1 m_2,n_1 n_2}(\mathbf{Q}=\mathbf{0};\Delta\mathbf{R}_{m_1 m_2},\Delta\mathbf{R}_{n_1 n_2}) \times\sum_{k'} e^{i\mathbf{k}'\cdot\Delta\mathbf{R}_{n_1 n_2}}e^{i\omega' 0^+}G_{n_1 n_2}(k'). \quad (17)$$

For the CuO_2 example, the nonzero sums collapse to

$$\Sigma^{(1H)}_{dd}(k)=U_{dd}\langle n_d\rangle+2U_{pd}(\langle n_x\rangle+\langle n_y\rangle),$$
$$\Sigma^{(1H)}_{xx}(k)=U_{pp}\langle n_x\rangle+2U_{pd}\langle n_d\rangle, \quad (18)$$
$$\Sigma^{(1H)}_{yy}(k)=U_{pp}\langle n_y\rangle+2U_{pd}\langle n_d\rangle,$$

with

$$\langle n_d\rangle=\frac{2T}{N}\sum_{k} e^{i\omega 0^+}G_{dd}(k) \quad (19)$$

and likewise for the other mean orbital occupancies.

The Fock contribution to the SCF (Fig. 9) is

$$\Sigma^{(1F)}_{m_1 m_2}(k)=-\frac{T}{N}\sum_{n_1 n_2}\sum_{\Delta\mathbf{R}_{m_1 m_2},\Delta\mathbf{R}_{n_1 n_2}} e^{-i\mathbf{k}\cdot\Delta\mathbf{R}_{m_1 m_2}} \times V^{\rm exc}_{m_1 m_2,n_1 n_2}(\mathbf{Q}=\mathbf{0};\Delta\mathbf{R}_{m_1 m_2},\Delta\mathbf{R}_{n_1 n_2}) \times\sum_{k'} e^{i\mathbf{k}'\cdot\Delta\mathbf{R}_{n_1 n_2}}e^{i\omega' 0^+}G_{n_1 n_2}(k'). \quad (20)$$

For the CuO_2 example,

$$\Sigma^{(1F)}_{dd}(k)=-\tfrac{1}{2}U_{dd}\langle n_d\rangle,$$
$$\Sigma^{(1F)}_{xx}(k)=-\tfrac{1}{2}U_{pp}\langle n_x\rangle,$$
$$\Sigma^{(1F)}_{dx}(k)=-U_{pd}\frac{T}{N}\sum_{k'}[1+e^{i(k'_x-k_x)}]e^{i\omega' 0^+}G_{dx}(k'), \quad (21)$$
$$\Sigma^{(1F)}_{xd}(k)=-U_{pd}\frac{T}{N}\sum_{k'}[1+e^{-i(k'_x-k_x)}]e^{i\omega' 0^+}G_{xd}(k').$$

Expressions for $\Sigma^{(1F)}_{yy}$, $\Sigma^{(1F)}_{dy}$, and $\Sigma^{(1F)}_{yd}$ follow by letting $x\rightarrow y$ in these equations.

Note that the Hartree and Fock terms may be neatly combined as

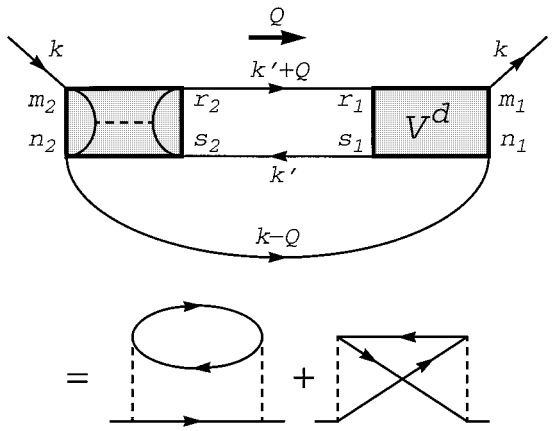

FIG. 10. Second-order correlation contributions $\Sigma^{(2)}_{m_1m_2}(k)$ to the one-particle SCF. Note that the use of the density vertex V^d allows writing these terms as a single diagram.

$$\Sigma^{(1)}_{m_1m_2}(k)=\frac{T}{N}\sum_{n_1n_2}\sum_{\Delta\mathbf{R}_{m_1m_2},\Delta\mathbf{R}_{n_1n_2}} e^{-i\mathbf{k}\cdot\Delta\mathbf{R}_{m_1m_2}} \times V^d_{m_1m_2,n_1n_2}(\mathbf{Q}=\mathbf{0};\Delta\mathbf{R}_{m_1m_2},\Delta\mathbf{R}_{n_1n_2}) \times\sum_{k'} e^{i\mathbf{k}'\cdot\Delta\mathbf{R}_{n_1n_2}}e^{i\omega'0^+}G_{n_1n_2}(k'), \quad (22)$$

where

$$V^d(\mathbf{Q})=2V^{\rm dir}(\mathbf{Q})-V^{\rm exc}(\mathbf{Q}). \quad (23)$$

The interaction V^d is just the coupling between density fluctuations (i.e., $S=0$ particle-hole pairs).

For second-order contributions to the SCF (Fig. 10), the corresponding expression is

$$\Sigma^{(2)}_{m_1m_2}(k)=\frac{T}{N}\sum_{n_1n_2}\sum_{\Delta\mathbf{R}_{m_1n_1},\Delta\mathbf{R}_{m_2n_2}} \times\sum_{Q} e^{-i(\mathbf{k}-\mathbf{Q})\cdot(\Delta\mathbf{R}_{m_1n_1}-\Delta\mathbf{R}_{m_2n_2})}G_{n_1n_2}(k-Q) \times(V^d\overline{\chi}V^{\rm dir})_{m_1n_1,m_2n_2}(Q;\Delta\mathbf{R}_{m_1n_1},\Delta\mathbf{R}_{m_2n_2}), \quad (24)$$

where

$$\overline{\chi}_{r_1s_1,r_2s_2}(Q;\Delta\mathbf{R}_{r_1s_1},\Delta\mathbf{R}_{r_2s_2})=-\frac{T}{N}\sum_{k'} e^{i\mathbf{k}'\cdot(\Delta\mathbf{R}_{r_1s_1}-\Delta\mathbf{R}_{r_2s_2})} \times G_{r_1r_2}(k'+Q)G_{s_2s_1}(k'), \quad (25)$$

and the product $V^d\overline{\chi}V^{\rm dir}$ is defined using the matrix multiplication

$$(AB)_{ab,cd}(Q;\Delta\mathbf{R}_{ab},\Delta\mathbf{R}_{cd})\equiv\sum_{ij}\sum_{\Delta\mathbf{R}_{ij}} A_{ab,ij}(Q;\Delta\mathbf{R}_{ab},\Delta\mathbf{R}_{ij}) \times B_{ij,cd}(Q;\Delta\mathbf{R}_{ij},\Delta\mathbf{R}_{cd}) \quad (26)$$

for general matrices A and B. Note that the use of the density interaction V^d allows grouping the two contributions from Fig. 10 in a single equation analogous to equation (2.30b) in Ref. 1.

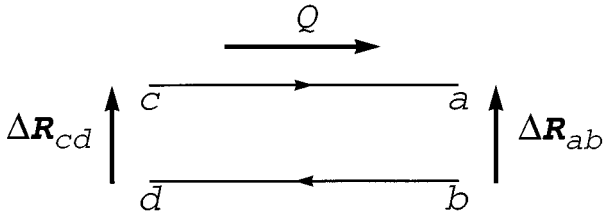

FIG. 11. Definition of unit-cell displacements and total momentum-frequency Q for the uncorrelated fluctuation propagator $\overline{\chi}_{ab,cd}(Q;\Delta\mathbf{R}_{ab},\Delta\mathbf{R}_{cd})$.

The quantity $\overline{\chi}_{ab,cd}(Q;\Delta\mathbf{R}_{ab},\Delta\mathbf{R}_{cd})$ is the uncorrelated fluctuation propagator for a particle-hole pair with total momentum-frequency Q; initial and final relative time displacement $\Delta\tau=0$; and initial and final relative unit-cell displacements $\Delta\mathbf{R}_{cd}$ and $\Delta\mathbf{R}_{ab}$, respectively (see Fig. 11):

$$\langle T_\tau c^\dagger_b(\mathbf{R}_b,\tau)c_a(\mathbf{R}_a,\tau)c^\dagger_c(\mathbf{R}_c,0)c_d(\mathbf{R}_d,0)\rangle^{\rm conn}_{\rm sc} =\frac{T}{N}\sum_Q e^{i(\mathbf{Q}\cdot\Delta\mathbf{R}_{ac}-\Omega\tau)}\overline{\chi}_{ab,cd}(Q;\Delta\mathbf{R}_{ab},\Delta\mathbf{R}_{cd}), \quad (27)$$

where the subscript ''sc'' denotes evaluation with the SCF action and

$$\langle\hat{O}_1(\tau)\hat{O}_2\rangle^{\rm conn}_{\rm sc}=\langle\hat{O}_1(\tau)\hat{O}_2\rangle_{\rm sc}-\langle\hat{O}_1\rangle_{\rm sc}\langle\hat{O}_2\rangle_{\rm sc}. \quad (28)$$

Note that the fluctuation propagator may be treated as a matrix in the combined space of particle-hole orbital indices ab and relative displacements $\Delta\mathbf{R}_{ab}$.

Finally the remaining particle-hole fluctuation contribution (see Fig. 12) to the FLEX SCF may be written

$$\Sigma^{(\rm ph)}_{m_1m_2}(k)=\frac{T}{N}\sum_{n_1n_2}\sum_{\Delta\mathbf{R}_{m_1n_1},\Delta\mathbf{R}_{m_2n_2}}\sum_Q \times e^{-i(\mathbf{k}-\mathbf{Q})\cdot(\Delta\mathbf{R}_{m_1n_1}-\Delta\mathbf{R}_{m_2n_2})}G_{n_1n_2}(k-Q) \times[\tfrac{1}{2}V^d(D-\overline{\chi})V^d +\tfrac{3}{2}V^m(M-\overline{\chi})V^m]_{m_1n_1,m_2n_2} \times(Q;\Delta\mathbf{R}_{m_1n_1},\Delta\mathbf{R}_{m_2n_2}), \quad (29)$$

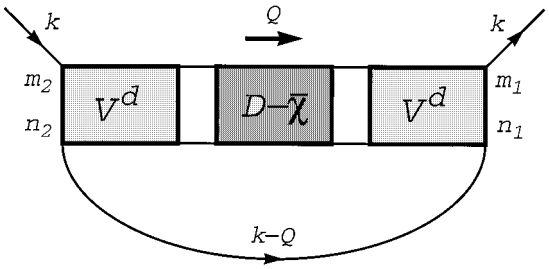

FIG. 12. Density fluctuation exchange contribution to the one-particle SCF. A similar term appears representing the exchange of magnetic fluctuations. Note that the fluctuation propagator is $D-\overline{\chi}$, rather than D. The subtraction prevents the double-counting of second-order terms.

TABLE I. Indexing scheme for the particle-hole basis set in the CuO_2 model. The particle orbital is a, the hole orbital is b, and the unit-cell displacement from hole to particle is $\Delta\mathbf{R}_{ab}$. The direct interaction vanishes except for states with indices 1–3, while the exchange interaction has nonzero matrix elements for all 11 indices.

Index	a	b	$\Delta\mathbf{R}_{ab}$
1	d	d	0
2	p_x	p_x	0
3	p_y	p_y	0
4	d	p_x	0
5	d	p_x	$+\hat{x}$
6	p_x	d	0
7	p_x	d	$-\hat{x}$
8	d	p_y	0
9	d	p_y	$+\hat{y}$
10	p_y	d	0
11	p_y	d	$-\hat{y}$

again employing shorthand notation for the matrix multiplication in Eq. (26). The matrix V^m is the coupling between magnetic fluctuations, and the matrices D and M are fluctuation propagators for density ($S=0$) and magnetic ($S=1$) fluctuations:

$$V^m(\mathbf{Q}) = -V^{\mathrm{exc}}(\mathbf{Q}), \tag{30}$$

and

$$\begin{aligned} D(Q) &= \overline{\chi}(Q)[1+V^d(\mathbf{Q})\overline{\chi}(Q)]^{-1}, \\ M(Q) &= \overline{\chi}(Q)[1+V^m(\mathbf{Q})\overline{\chi}(Q)]^{-1}. \end{aligned} \tag{31}$$

In order to perform calculations for a model with short-range interactions, it is convenient to enumerate all combinations of the compound orbital index ab and displacement vector $\Delta\mathbf{R}_{ab}$ for which matrix elements of $V^d(\mathbf{Q})$ or $V^m(\mathbf{Q})$ are nonzero. For the CuO_2 model there are only 11 such combinations, and the particle-hole interactions and fluctuation propagators may be stored compactly as 11×11 matrices. One possible indexing scheme is indicated in Table I. With this choice of basis, the interaction matrices are as follows:

$$\begin{aligned} V^d(\mathbf{Q})_{11} &= U_{dd}, \\ V^d(\mathbf{Q})_{22} &= V^d(\mathbf{Q})_{33} = U_{pp}, \\ V^d(\mathbf{Q})_{12} &= V^d(\mathbf{Q})^*_{21} = 2U_{pd}(1+e^{-iQ_x}), \\ V^d(\mathbf{Q})_{13} &= V^d(\mathbf{Q})^*_{31} = 2U_{pd}(1+e^{-iQ_y}), \\ V^d(\mathbf{Q})_{ii} &= -U_{pd}, \quad i=4,5,\ldots,11, \end{aligned} \tag{32}$$

and

$$\begin{aligned} V^m(\mathbf{Q})_{11} &= -U_{dd}, \\ V^m(\mathbf{Q})_{22} &= V^m(\mathbf{Q})_{33} = -U_{pp}, \\ V^m(\mathbf{Q})_{ii} &= -U_{pd}, \quad i=4,5,\ldots,11. \end{aligned} \tag{33}$$

Note that $\mathbf{Q}$ is measured in units of the inverse lattice constant.

III. SOME DETAILS OF THE SOLUTION ALGORITHM

The FLEX solution of the CuO_2 model may be divided into four computational steps: (i) calculation of the uncorrelated fluctuation propagators $\overline{\chi_{ij}}(\mathbf{Q},i\Omega)$ as convolutions of the one-particle propagator G_{ab}; (ii) matrix inversion to find the correlated fluctuation propagators $M_{ij}(\mathbf{Q},i\Omega)$ and $D_{ij}(\mathbf{Q},i\Omega)$; (iii) calculation of the one-particle SCF matrix $\Sigma_{ab}(\mathbf{k},i\omega)$; and (iv) matrix inversion to find the one-particle propagator $G_{ab}(\mathbf{k},i\omega)$. Note that the indices i and j run over 11 values, while a and b run over only 3.

The most time-consuming steps are the convolutions used to evaluate $\overline{\chi_{ij}}$ and Σ_{ab}. Fast Fourier transforms may be used for this purpose.[4] However, we have found it efficient to proceed using a combination of methods applied to one-orbital models in our earlier work.[5,6,10] The frequency-space renormalization group introduced in Ref. 5 is applicable in the present study with only minor modifications.

Rather than accumulating two scalar functions $\Delta\Sigma$ and $\Delta\overline{\chi}$ to account for renormalization corrections from regions of high frequency, it is necessary to generalize to matrix functions $\Delta\Sigma_{ab}$ and $\Delta\overline{\chi_{ij}}$. In addition we have modified the previous algorithm in two ways to gain improved accuracy. These modifications are as follows: (i) improved interpolation, and (ii) special treatment of the first-order self-energy $\Sigma^{(1)}$. Previously piecewise linear interpolation and extrapolation have been used to carry $\Delta\Sigma$ and $\Delta\overline{\chi}$ from one Matsubara frequency mesh to a finer mesh for use at reduced temperature. In the present work piecewise quadratic interpolation and extrapolation are found to be superior. Particular care is required in the vicinity of the dividing point between ''high'' and ''low'' renormalization regions. When interpolating $\Delta\Sigma$ onto the new ''low'' region mesh, we have found it preferable to use only ''low'' region data. The only exception is for points which lie between the highest frequency in the ''low'' region and the lowest frequency in the ''high'' region; in this case a single point from the ''high'' region should be used in the interpolation. Similar care must be exercised in the interpolation of $\Delta\overline{\chi}$ to avoid slope discontinuities associated with the multistage fermion cutoffs.

The second modification of previous algorithms concerns the treatment of the first-order self-energy. This quantity generates a temperature-dependent, instantaneous term in the self-consistent action functional. To calculate a smooth propagator it is essential that the *same* first-order self-energy appear in all frequency components. This means that $\Sigma^{(1)}$ cannot be ''folded down'' using a standard frequency-space renormalization group. (In single-orbital models the first-order self-energy may be absorbed into the chemical potential, leaving only a frequency-dependent self-energy which vanishes for $\omega\to\infty$. This redefinition of the action is not possible for multiorbital models, in which $\Sigma^{(1)}$ is a matrix.) In fact, we have found within the CuO_2 FLEX solution (see Sec. IV) that $\Sigma^{(1)}$ varies little with temperature below $T/t_{pd}=0.25$. (The variation is smallest near $\langle n\rangle=1$ and increases as $\langle n\rangle$ varies from unity.) In order to take into account this variation, we have found it convenient (a) to delay commencing the renormalization group until $T/t_{pd}=0.25$,

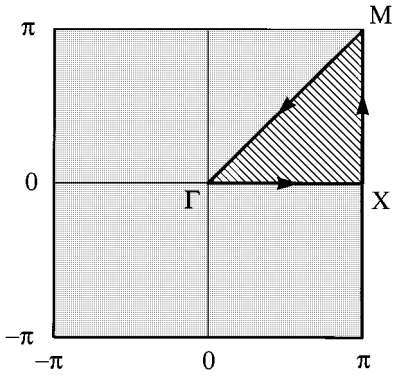

FIG. 13. Irreducible wedge in the square-lattice Brillouin zone. The wave vector is measured in units of the inverse lattice constant a^{-1}.

and (b) to calculate $\Sigma^{(1)}(T)$ without the aid of the renormalization procedure, i.e., by summing the propagator over all frequencies. (This calculation adds little to the overall computational overhead.) For the frequency-dependent parts of the self-energy, renormalization proceeds as before, i.e., regions of frequency space are sequentially eliminated with decreasing temperature. It is interesting to note that, while the results we report in Sec. IV are calculated with fixed chemical potential, this modified renormalization-group scheme makes it possible to calculate accurately for fixed density as well.

A final note is in order concerning the Fourier transform of renormalized quantities, including $G(\mathbf{k},i\omega)$. Before summing on frequency it is essential to interpolate such quantities onto a *uniform* mesh corresponding to the current temperature. Otherwise, the resulting Fourier transform is contaminated by ripples arising from the breaks in mesh scale.

An additional calculational detail is the use of discrete rotational symmetry to reduce the size of the computation with respect to spatial variables. For the square CuO_2 lattice, the quantities Σ, G, $\overline{\chi}$, and χ may be calculated for $\mathbf{k}$ and $\mathbf{Q}$ restricted to a triangular wedge in the first Brillouin zone (see Fig. 13), then extended to the full zone by symmetry operations. Note that some care is required since the indices ab and ij must be transformed along with the wave vectors $\mathbf{k}$ and $\mathbf{Q}$. In addition to changes in the orbital labels and the relative separation of particle-hole pairs, changes in the center-of-mass (CM) unit-cell position may be induced by symmetry operations. For example, under rotation by π, the p_x orbital in the unit cell with origin $\mathbf{R}$ maps to the p_x orbital in the unit cell with origin $\mathbf{R}-\hat{x}$. This translation by one unit cell with respect to the original basis induces an extra phase $\exp(\pm i\mathbf{k}\cdot\hat{x})$ in the symmetry relation for the propagator $G(\mathbf{k})$.

One might also be concerned about the possible appearance of minus signs associated with a change in phase of orbitals after a symmetry operation. Since (i) orbitals always appear in *pairs* in the correlation functions of interest and (ii) the convention for orbital phases has been chosen so that all orbitals pick up the same sign after application of a symmetry operation, extra minus signs do not appear.

With these points noted, the symmetry relations may be stated as follows: Suppose that a general point $\mathbf{k}'$ ($\mathbf{Q}'$) in the Brillouin zone maps to a point $\mathbf{k}$ ($\mathbf{Q}$) in the irreducible wedge (Fig. 13) after applying symmetry operations (inversion, rotation, reflection, or a combination of these). Let a and b (i and j) represent the orbital (orbital pair and relative separation) labels for a correlation function evaluated at $\mathbf{k}'$ ($\mathbf{Q}'$), with sym(a) and sym(b) [sym(i) and sym(j)] the corresponding labels for the point in the wedge. Let the CM translations corresponding to this symmetry operation be $\delta\mathbf{R}_a$ and $\delta\mathbf{R}_b$ ($\delta\mathbf{R}_i$ and $\delta\mathbf{R}_j$). Then

$$G_{ab}(\mathbf{k}',i\omega)=e^{i\mathbf{k}\cdot(\delta\mathbf{R}_a-\delta\mathbf{R}_b)}G_{\mathrm{sym}(a),\mathrm{sym}(b)}(\mathbf{k},i\omega) \quad (34)$$

and

$$\chi_{ij}(\mathbf{Q}',i\Omega)=e^{i\mathbf{Q}\cdot(\delta\mathbf{R}_i-\delta\mathbf{R}_j)}\chi_{\mathrm{sym}(i),\mathrm{sym}(j)}(\mathbf{Q},i\Omega). \quad (35)$$

Corresponding relations hold for the matrices Σ and $\overline{\chi}$.

As an example, consider a point with $Q_x'=-Q_y$ and $Q_y'=-Q_x$, where $\mathbf{Q}$ is in the irreducible wedge. The symmetry operation which carries $\mathbf{Q}'$ onto $\mathbf{Q}$ is inversion, followed by reflection across $x=y$. If $i=6$ and $j=11$ (see Table I), then it may be shown that $\mathrm{sym}(i)=11$, $\mathrm{sym}(j)=6$, $\delta\mathbf{R}_i=-\hat{y}$, and $\delta\mathbf{R}_j=-\hat{x}$. Thus,

$$\chi_{6,11}(-Q_y,-Q_x,i\Omega)=e^{i(Q_x-Q_y)}\chi_{11,6}(Q_x,Q_y,i\Omega). \quad (36)$$

For a 16×16 $\mathbf{k}$-space discretization, the number of grid points to be calculated is reduced using symmetry operations from 256 to 45, a factor of nearly 6. For finer discretizations, a renormalization group treatment of the $\mathbf{k}$ space (or a fast Fourier transform algorithm[4]) would eventually become essential.

As a final point we note the criteria employed for declaring convergence of the FLEX equations. Let $G^{(n)}$ be the one-particle propagator at the end of the nth iteration. The equations are assumed to be converged to self-consistency when, for every matrix element and value of k, (i) the absolute error $|G^{(n+1)}-G^{(n)}|$ is less than a tolerance $\varepsilon_{\mathrm{abs}}$; *or* (ii) the relative error $|G^{(n+1)}-G^{(n)}|/|G^{(n+1)}|$ is less than a tolerance $\varepsilon_{\mathrm{rel}}$. We have chosen the values $\varepsilon_{\mathrm{abs}}=1\times10^{-6}$ and $\varepsilon_{\mathrm{rel}}=1\times10^{-4}$ throughout.

IV. RESULTS AND DISCUSSION

In this section we describe results from FLEX calculations for the three-band CuO_2 model used frequently to treat the high-temperature superconductors.[12] This model describes a two-dimensional square Bravais lattice with one Cu ion and two O ions per unit cell (see Fig. 5). A single tight-binding orbital is retained on each ion in order to describe the dominant parentage of Fermi surface particles. These orbitals are (a) the $3d_{x^2-y^2}$ for Cu ions; (b) the $2p_x$ for O ions on horizontal bonds; and (c) the $2p_y$ for O ions on vertical bonds. In the high-temperature superconductors the three orbitals are nearly filled, and it is conventional to write the Hamiltonian using creation operators $c^\dagger$ for holes. (To maintain continuity with the general discussion in Sec. II we continue to refer to the states created by $c^\dagger$ as ''particles,'' rather than as holes or electrons.) The density range of interest is $\langle n\rangle$ of order unity, i.e., one hole per unit cell. For $\langle n\rangle$ less than unity, the system is said to be ''electron-doped''; for $\langle n\rangle$ greater than unity, ''hole-doped.''

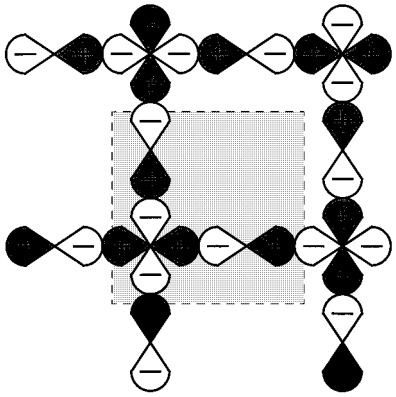

FIG. 14. Choice of phases for the Cu $3d_{x^2-y^2}$, O $2p_x$, and O $2p_y$ orbitals in the CuO_2 model.

It is convenient[22] to choose the orbital phases in the checkerboard pattern of Fig. 14, so that corresponding orbitals in adjacent horizontal or vertical cells differ in phase by -1. With this choice the nearest-neighbor transfer integrals are all equal. In the notation of Eq. (1),

$$h^0_{xd}(\mathbf{R},\mathbf{R}) = h^0_{dx}(\mathbf{R},\mathbf{R}) = h^0_{xd}(\mathbf{R},\mathbf{R}+\hat{x}) = h^0_{dx}(\mathbf{R}+\hat{x},\mathbf{R}) \equiv -t_{pd}, \tag{37}$$

with t_{pd} a positive number (in the hole Hamiltonian). A similar relation holds for h^0_{yd} and h^0_{dy}. It is trivial to allow an O-O transfer integral t_{pp} in addition; note that with the phase convention in Fig. 14, t_{pp} has the same sign as t_{pd}. Thus,

$$h^0_{yx}(\mathbf{R},\mathbf{R}) = h^0_{yx}(\mathbf{R}+\hat{x},\mathbf{R}) = h^0_{yx}(\mathbf{R}+\hat{x}-\hat{y},\mathbf{R}) = h^0_{yx}(\mathbf{R}-\hat{y},\mathbf{R}) \equiv -t_{pp}, \tag{38}$$

and so forth.

It is important to note how our choice of orbital phases affects the one-particle band structure. An alternative to the checkerboard pattern is the choice of a uniform phase in all unit cells (so that the positive lobes of all $2p_x$ orbitals point to the right, for instance). It is straightforward to show that the values of $\mathbf{k}$ labeling the same one-particle state within the checkerboard and uniform phase schemes differ by (π,π). In other words, the Γ point (Brillouin zone center) within our calculation corresponds to the M point (Brillouin zone corner) within the alternative labeling scheme; a rigid shift of (π,π) along the zone diagonal transforms one band structure into the other. Note, however, that the total wave vector $\mathbf{Q}$ of particle-hole and particle-particle pair states is *identical* within the two schemes.

The ''on-site'' terms in h^0 (which do not depend on the orbital phases) may be written

$$h^0_{dd}(\mathbf{R},\mathbf{R}) \equiv \varepsilon_d, \qquad h^0_{xx}(\mathbf{R},\mathbf{R}) = h^0_{yy}(\mathbf{R},\mathbf{R}) \equiv \varepsilon_p = \varepsilon_d + \varepsilon. \tag{39}$$

The full one-particle Hamiltonian takes the form

$$\begin{aligned}\hat{H}_0 - \mu N = {} & (\varepsilon_d - \mu)\sum_{\mathbf{R}} n_d(\mathbf{R}) + (\varepsilon_d - \mu + \varepsilon)\sum_{\mathbf{R}} [n_x(\mathbf{R}) \\ & + n_y(\mathbf{R})] - t_{pd}\sum_{\sigma,\mathbf{R}} [c^\dagger_{d\sigma}(\mathbf{R})c_{x\sigma}(\mathbf{R}) \\ & + c^\dagger_{d\sigma}(\mathbf{R}+\hat{x})c_{x\sigma}(\mathbf{R}) + c^\dagger_{d\sigma}(\mathbf{R})c_{y\sigma}(\mathbf{R}) \\ & + c^\dagger_{d\sigma}(\mathbf{R}+\hat{y})c_{y\sigma}(\mathbf{R}) + \text{H.c.}] \\ & - t_{pp}\sum_{\sigma,\mathbf{R}} [c^\dagger_{y\sigma}(\mathbf{R})c_{x\sigma}(\mathbf{R}) + c^\dagger_{y\sigma}(\mathbf{R}+\hat{x})c_{x\sigma}(\mathbf{R}) \\ & + c^\dagger_{y\sigma}(\mathbf{R}-\hat{y})c_{x\sigma}(\mathbf{R}) + c^\dagger_{y\sigma}(\mathbf{R}+\hat{x}-\hat{y})c_{x\sigma}(\mathbf{R}) \\ & + \text{H.c.}].\end{aligned} \tag{40}$$

It is more convenient to work with the Fourier-transformed Hamiltonian

$$\hat{H}_0 - \mu N = \sum_{\sigma}\sum_{ab}\sum_{\mathbf{k}} [h^0_{ab}(\mathbf{k}) - \mu\delta_{ab}]c^\dagger_{a\sigma}(\mathbf{k})c_{b\sigma}(\mathbf{k}), \tag{41}$$

where

$$h^0(\mathbf{k}) = \begin{bmatrix} \varepsilon_d & -t_{pd}(1+e^{-ik_x}) & -t_{pd}(1+e^{-ik_y}) \\ -t_{pd}(1+e^{ik_x}) & \varepsilon_d+\varepsilon & -t_{pp}(1+e^{ik_x})(1+e^{-ik_y}) \\ -t_{pd}(1+e^{ik_y}) & -t_{pp}(1+e^{-ik_x})(1+e^{ik_y}) & \varepsilon_d+\varepsilon \end{bmatrix}, \tag{42}$$

with the states labeled $d\to 1$, $x\to 2$, and $y\to 3$.

As discussed in Sec. II, the Coulomb interaction in the CuO_2 model is usually truncated at near-neighbor separation. Three different Coulomb integrals U_{dd}, U_{pp}, and U_{pd} are retained, as in Eq. (10).

We begin our discussion of the CuO_2 FLEX solution with brief sections on $\mathbf{k}$-space discretization error (Sec. IV A) and error from the use of the frequency-space renormalization group (Sec. IV B). We then examine the most unstable channels in the 11×11 zero-frequency fluctuation propagators for magnetic and density fluctuations (Sec. IV C). We survey Hartree-Fock and FLEX results for the one-particle band structure in Sec. IV D and plot the orbital occupancy factors $n_{ab}(\mathbf{k})$ in Sec. IV E. Finally we discuss results for the real-frequency spectral densities corresponding to one-particle excitations (Sec. IV F) and particle-hole fluctuations (Sec. IV G).[23]

Throughout these sections we refer to a ''standard parameter set'' based on the constrained-occupancy LDA calculations of Hybertsen, Schlüter, and Christensen[24] for La_2CuO_4. Energies are measured in units of the nearest-neighbor transfer integral t_{pd}, and the $3d_{x^2-y^2}$ on-site energy ϵ_d is set to

zero. The ''standard parameter set'' is as follows:

$$
\begin{aligned}
t_{pd} &\simeq 1.3 \text{ eV}, \\
\varepsilon &\simeq 3.6 \text{ eV} = 2.75 t_{pd}, \\
t_{pp} &\simeq 0.65 \text{ eV} = 0.5 t_{pd}, \\
U_{dd} &\simeq 10.5 \text{ eV} = 8 t_{pd}, \\
U_{pp} &\simeq 4 \text{ eV} = 3 t_{pd}, \\
U_{pd} &\simeq 1.2 \text{ eV} = t_{pd}.
\end{aligned}
\tag{43}
$$

We examine particle densities corresponding to both ''electron doping'' ($\langle n \rangle$ less than 1) and ''hole doping'' ($\langle n \rangle$ greater than 1). For comparison with other studies, note the comment on orbital phases and **k**-space band structure at the beginning of this section.

IV. CuO_2 FLEX SOLUTION

A. Discretization error

In this paper we predominantly employ 8×8 and 16×16 discretizations of the square Brillouin zone to solve the FLEX equations. In Fig. 15 results for the τ-dependent one-particle propagators $G_{dd}(\mathbf{k},\tau)$ and $G_{xx}(\mathbf{k},\tau)$ are compared for calculations on a 4×4, 8×8, and 16×16 mesh using the standard parameter set. The wave vector $\mathbf{k}=(\pi/2,\pi/2)$ is chosen to lie near the Fermi surface for $\langle n \rangle = 0.875$ (electron doping). The temperature is $T/t_{pd}=0.016$.

A similar comparison for the magnetic particle-hole propagator $M_{11}(\mathbf{Q},\tau)$ is shown in Fig. 16. The wave vector $\mathbf{Q}=(\pi,\pi)$, and other parameters are as in Fig. 15. It is useful to split this propagator into ''dc'' and time-dependent components using Eqs. (27) and (31):

$$
M_{11}(\mathbf{Q},\tau) \equiv T M_{11}(\mathbf{Q},\Omega=0) + \Delta M_{11}(\mathbf{Q},\tau). \tag{44}
$$

The time-dependent component [Fig. 16(a)], like the one-particle propagator, is only weakly dependent on the discretization scale. The dc component has a much stronger variation with the discretization scale at low temperatures [Fig. 16(b)]. This variation is expected (at least within the FLEX approximation), since the static magnetic response at $\mathbf{Q}=(\pi,\pi)$ is divergent for $T\rightarrow 0$. Note that the scale dependence at this single point in **Q** space is only weakly reflected in other components of the one-particle and particle-hole propagators.

For the temperatures studied in this paper ($T/t_{pd} \geqslant 0.016$) the maximum error in working with an 8×8 rather than a 16×16 discretization is of order 0.5% for the one-particle propagator and 2% for the particle-hole propagator (with the exception of the divergent dc magnetic component discussed above). The results in Secs. IV D–IV F are obtained exclusively for a 16×16 discretization.

B. Renormalization-group error

As discussed in Sec. III, the frequency-space renormalization group (RG) introduced in Ref. 5 is used to reduce computational time and storage requirements. The RG procedure is approximate and introduces errors which must be monitored. In Fig. 17 we compare results for the propagators $G_{dd}(\mathbf{k},\tau)$ and $G_{xx}(\mathbf{k},\tau)$ for an 8×8 **k**-space mesh, a simplified parameter set with $U_{pp}=U_{pd}=0$, $\langle n \rangle = 0.875$ (electron doping), $T/t_{pd}=0.031$, and $\mathbf{k}=(\pi/2,\pi/2)$. The results were obtained first using a full brute-force solution, then using a five-step renormalization group. Both the full and the renormalization-group solutions assume a frequency-space cutoff at $\Omega/t_{pd}=\pm 50$. The corresponding result for the magnetic particle-hole propagator $\Delta M_{11}(\mathbf{Q},\tau)$ with $\mathbf{Q}=(\pi,\pi)$ is plotted in Fig. 18. For the range of temperatures studied in this paper we estimate the maximum error introduced by the frequency-space renormalization group to be of order 1% for one-particle and nonsingular two-particle propagators and 5% for the singular magnetic propagator.

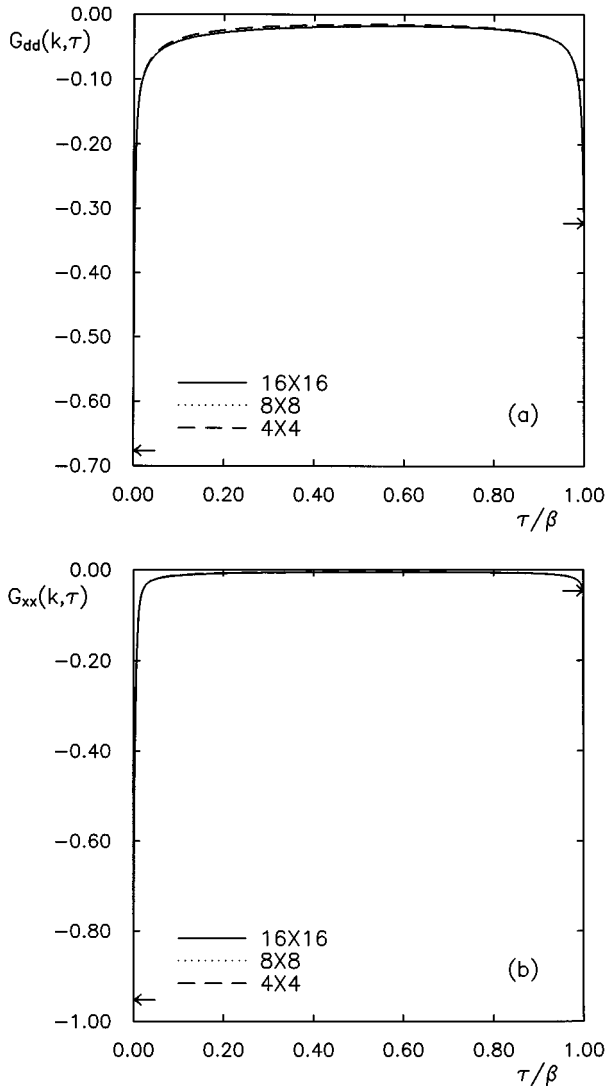

FIG. 15. Effect of lattice discretization on one-particle propagators G in the CuO_2 model. The standard parameter set [Eq. (43)] is employed with $\langle n \rangle = 0.875$ (electron doping) and $T/t_{pd}=0.016$. Results are shown for wave vector $\mathbf{k}=(\pi/2,\pi/2)$. Arrows indicate the intercepts at $\tau=0^+$ and $\tau=\beta^-$. (a) G_{dd}. (b) G_{xx}.

C. Eigenvalues of the fluctuation kernel

The FLEX approximation is framed to describe the exchange of particle-hole fluctuations between one-particle ex-

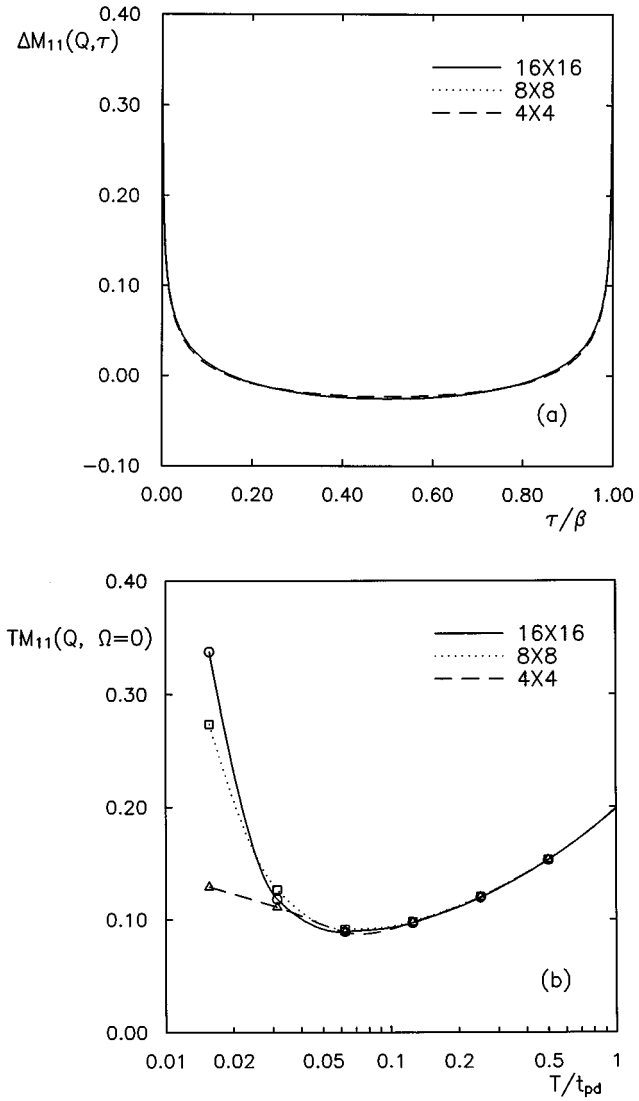

FIG. 16. Effect of lattice discretization on the d-orbital-projected magnetic particle-hole propagator M_{11}. Parameters are as in Fig. 15, and the wave vector $\mathbf{Q}=(\pi,\pi)$. (a) Time-dependent part of the propagator $\Delta M_{11}(\mathbf{Q},\tau)$. (b) Zero-frequency component of the propagator $TM_{11}(\mathbf{Q},\Omega=0)$.

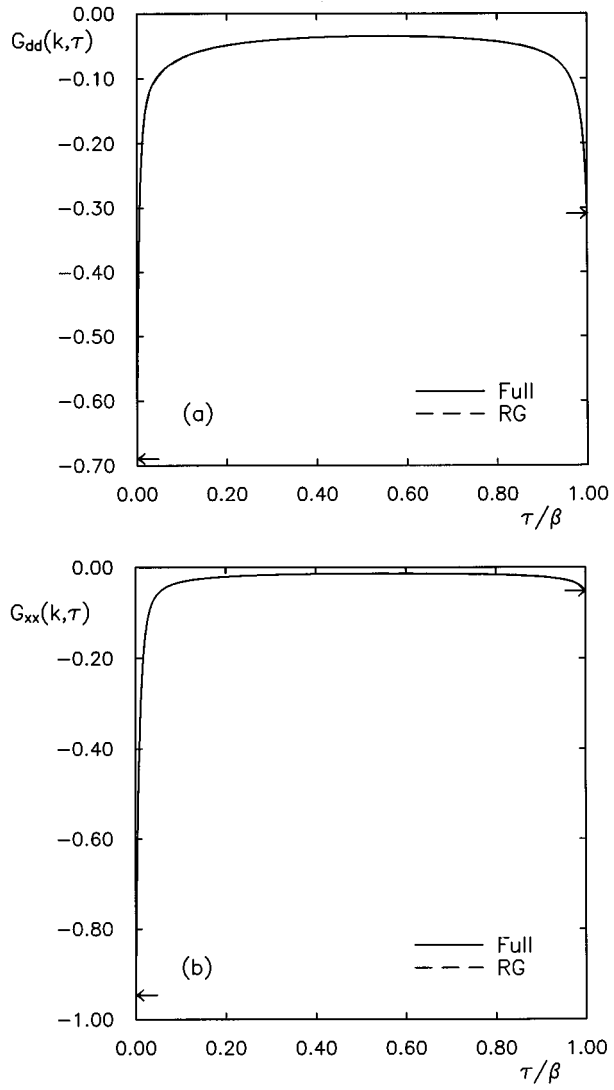

FIG. 17. Validation of renormalization-group calculations for the one-particle propagator G. A simplified parameter set is employed with $U_{pp}=U_{pd}=0$, and other parameters set to their standard values. The lattice discretization is 8×8, with $\langle n\rangle=0.875$ (electron doping) and $T/t_{pd}=0.031$. Results from a full brute-force calculation are compared with results from a five-stage renormalization group. The wave vector $\mathbf{k}=(\pi/2,\pi/2)$. (a) G_{dd}. (b) G_{xx}.

citations. In the model treated here, particle-hole correlations are instantaneous, and the $S=0$ and $S=1$ propagators are 11×11 matrices in the combined space of orbital labels and unit-cell separations. It is of interest to determine the fluctuation ''channel'' which becomes most unstable as the system temperature decreases. The nature of the FLEX approximation assures that the correlated propagators do not develop actual singularities at finite temperature. Nevertheless for most parameter sets a single magnetic or density channel dominates the low-temperature physics, altering the lifetime of one-particle excitations and biasing the nature of a potential superconducting state. The identity of the dominant fluctuation channel has been a subject of past debate,[18–20,25–29] particularly with regard to the effect of the near-neighbor Coulomb integral U_{pd}. At issue has been the competition between a large-$\mathbf{Q}$, $S=1$ channel (an antiferromagnetic $3d_{x^2-y^2}$ spin fluctuation) and a $\mathbf{Q}=0$, $S=0$ channel (a uniform density fluctuation involving charge transfer from $3d_{x^2-y^2}$ to $2p_x$ and $2p_y$ orbitals).

The particle-hole fluctuations may be monitored quantitatively by diagonalizing the 11×11 matrices (see Sec. II) $-V^d(\mathbf{Q})\overline{\chi}(Q)$ and $-V^m(\mathbf{Q})\overline{\chi}(Q)$, after iterating the FLEX equations to self-consistency. The dominant instabilities always occur for $\Omega=0$; further, by symmetry, it is only necessary to consider $\mathbf{Q}$ in an irreducible Brillouin zone wedge (see Sec. III). The dominant channel is the eigenvector with the most positive eigenvalue. Note, as discussed above, that all finite-temperature FLEX eigenvalues are smaller than unity (though an eigenvalue may smoothly approach unity with decreasing temperature).

It is important to note that the eigenvalues determined in this way are *not* the same as the instability eigenvalues calculated in previous studies of superconductivity in Hubbard-like models.[2,6–10] To calculate conserving susceptibilities within FLEX one must first determine the appropriate irreducible vertex functions.[1] Since FLEX is not consistent at

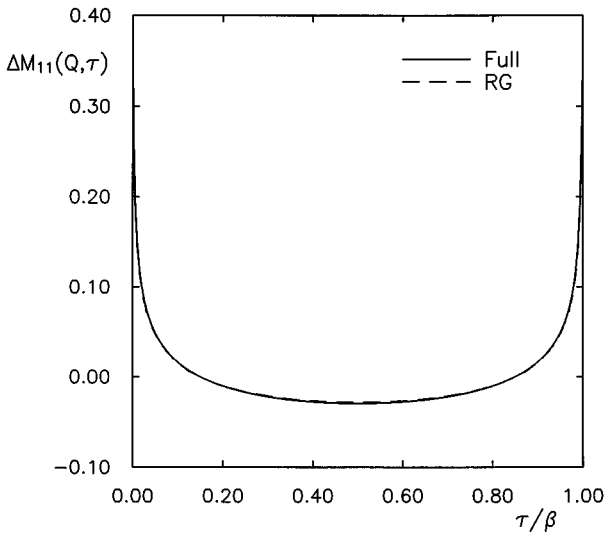

FIG. 18. Validation of renormalization-group calculations for the time-dependent part of the magnetic particle-hole propagator ΔM_{11}. Parameters are as in Fig. 17. The wave vector $\mathbf{Q}=(\pi,\pi)$.

the two-particle level, these functions differ from the input interactions. (For example, in this paper we neglect particle-particle interactions in calculating one-particle SCF's. Nevertheless, the resulting particle-particle susceptibilities are nontrivial and may show a tendency toward superconductivity.) Vertex corrections do not appear in the fluctuation propagators which enter the one-particle SCF calculation. [Note that in FLEX calculations for the one-band Hubbard model, the eigenvalue calculation discussed here is trivial: The magnetic and density kernels become 1×1 matrices with eigenvalues $\pm U\overline{\chi}(\mathbf{Q},\Omega=0)$.]

In order to describe the physics of the competing channels, it is convenient to speak somewhat loosely of ''particle-hole binding.'' In fact, no actual binding instability occurs (at least in the FLEX propagators), only resonant scattering. From Eqs. (32) and (33) it is clear that the most attractive interaction matrix element for the standard parameter set is $V^m(\mathbf{Q})_{11}$, which scatters an $S=1$ on-site d-d particle-hole pair into itself. The wave vector for binding is determined by the particle-hole density of states, which enters the calculation through the uncorrelated propagator matrix $\overline{\chi}(\mathbf{Q},\Omega=0)$. For the square lattice with $\langle n\rangle$ close to unity, this suggests binding in a large-$\mathbf{Q}$, $S=1$ state with dominant d-d parentage. The amount of admixture of the other ten particle-hole basis states is determined by the relative size of U_{pp} and U_{pd}. [It is interesting to note that for $\mathbf{Q}=(\pi,\pi)$ the matrix $\overline{\chi}$ has a special symmetry which results in the exact vanishing of the p_x-p_x and p_y-p_y components of the dominant eigenvector.]

In the density matrix $V^d(\mathbf{Q})$ the only matrix elements with an attractive real part occur on the diagonal, scattering mixed-orbital particle-hole states (such as an intracell d particle and p_x hole) into themselves. For the standard parameter set these matrix elements are small in comparison with those in the $S=1$ channel, and magnetism is expected to dominate. Nevertheless, the presence of negative diagonal matrix elements in the $S=0$ interaction matrix suggests that at least one density channel is enhanced, rather than suppressed, by the Coulomb interaction. Naive arguments based on the particle-hole density of states (at least for $\epsilon\sim0$) again suggest binding at large $\mathbf{Q}$. In comparison, the density channel in the one-band Hubbard model is always suppressed.[2,3]

The charge-transfer channel, which has been the subject[18–20,25–29] of several previous studies, is not superficially evident from the form of the interaction matrix. It depends on the presence of the off-diagonal matrix elements $V^d(\mathbf{Q})_{12}$ and $V^d(\mathbf{Q})_{13}$. These matrix elements vanish at $Q_x=Q_y=\pi$ and are maximized for $Q_x=Q_y=0$ at a value of $4U_{pd}$. Their presence allows the formation of a bound state containing d-d and p-p components with *opposite* sign. The density-wave order parameter corresponding to this eigenvector has a charge deficit in the d orbitals and a charge surplus in the p orbitals: such an order parameter reduces the repulsive Coulomb energy contributed by particles on adjacent sites. The fact that the off-diagonal matrix elements are maximized for $\mathbf{Q}=\mathbf{0}$ insures that the most unstable charge-transfer channel is uniform, not staggered. (Note that a bound state also arises due to repulsive off-diagonal matrix elements in treatments of d-wave superconductivity[2,6–10] in the one-band Hubbard model.)

To determine the dominant fluctuation channel for a wide range of parameters in the CuO_2 model, we have performed a survey starting from the standard parameter set for both hole doping ($\langle n\rangle=1.125$) and electron doping ($\langle n\rangle=0.875$). Detailed results are reported here for the hole-doped case. Results for electron doping are qualitatively quite similar, and the conclusions reached below survive intact. The temperature T/t_{pd} is fixed at $1/64\sim0.016$, a value sufficiently low to yield the correct eigenvalue order for $T\to0$. (The eigenvalue order in some cases changes at high temperatures.) The $\mathbf{k}$-space discretization scale is 8×8. In the plots below we indicate the maximum eigenvalues of the magnetic and density kernels on a logarithmic scale based on the deviation from unity. This scale allows a close examination of the behavior of nearly singular eigenvalues.

In Fig. 19 the variation of the maximum magnetic and density channel eigenvalues, λ_m and λ_d, as a function of the bare level separation ε is plotted for three values of U_{pd}, the near-neighbor repulsion. Note that for $U_{pd}=0$ there is no attractive density eigenvalue. For $U_{pd}/t_{pd}=1$ (including the standard parameter set), the most attractive density channel is a $\mathbf{Q}=\mathbf{0}$ mixed-orbital state. As noted above, one might have guessed the preferred wave vector would be (π,π), based on density-of-states effects alone. (The density eigenvalue's dependence on $\mathbf{Q}$ is in fact very weak in this case.) Only for $U_{pd}/t_{pd}=4$ is the dominant density channel the charge-transfer state. The wave vector of this state is $\mathbf{Q}=\mathbf{0}$, as expected, for $\varepsilon/t_{pd}\geqslant0.5$. [For smaller ε, the wave vector shifts away from 0 toward $(\pi/2,\pi/2)$, though the dependence on $\mathbf{Q}$ is weak.] As an example, for $U_{pd}/t_{pd}=4$ and $\varepsilon/t_{pd}=1$, the normalized eigenvector ϕ has

$$\begin{gathered}\mathbf{Q}=\mathbf{0},\\ |\langle 1|\phi\rangle|^2=0.722,\\ |\langle 2|\phi\rangle|^2=|\langle 3|\phi\rangle|^2=0.135,\\ |\langle m|\phi\rangle|^2=0.001,\quad m=4,\ldots,11.\end{gathered}\tag{45}$$

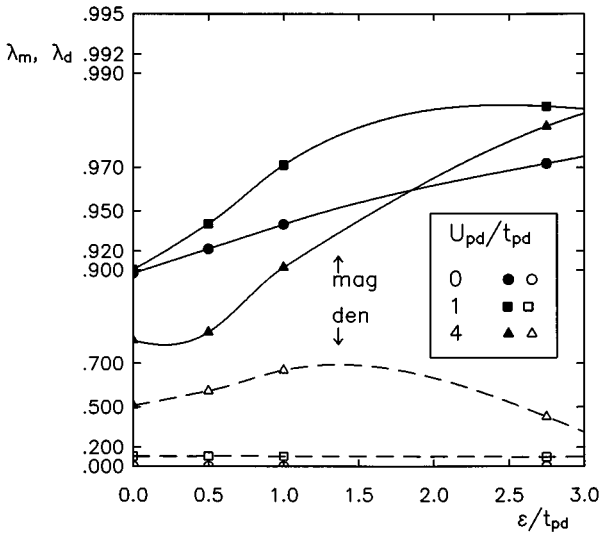

FIG. 19. Maximum magnetic and density channel eigenvalues of the FLEX interaction kernel, λ_m and λ_d, as a function of bare level separation ε/t_{pd}. Results are shown for three values of U_{pd}/t_{pd}, with other parameters set at their standard values. The particle density is $\langle n\rangle = 1.125$ (hole doping), and the temperature is fixed at $T/t_{pd} = 0.016$. Solid lines and closed symbols represent magnetic eigenvalues; dashed lines and open symbols represent density eigenvalues. The eigenvalue axis is logarithmic in the deviation from unity. See the text for identification of the eigenvectors.

The $\langle 2|\phi\rangle$ and $\langle 3|\phi\rangle$ matrix elements are equal and have the opposite sign from $\langle 1|\phi\rangle$. (Refer to Table I for identification of the basis states.) The important point to note is that even for $U_{pd}/t_{pd} = 4$ (i.e., $U_{pd}/U_{dd} = 0.5$) the charge-transfer eigenvalue remains significantly smaller than the magnetic eigenvalue at low temperatures. Only for large T/t_{pd} (Fig. 20)

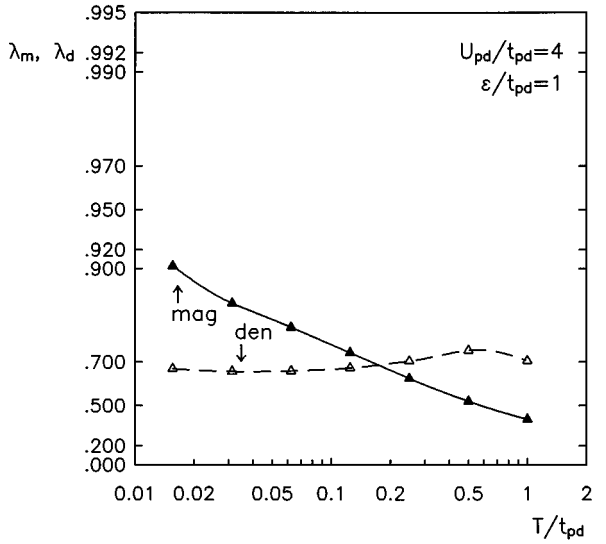

FIG. 20. Temperature variation of the maximum magnetic and density channel eigenvalues. The values of U_{pd}/t_{pd} and ε/t_{pd} are set to 4 and 1, enhancing the Cu-O charge-transfer process. Other parameters are as in Fig. 19. Note that the magnetic channel dominates up to a temperature of order $T/t_{pd} = 0.15$.

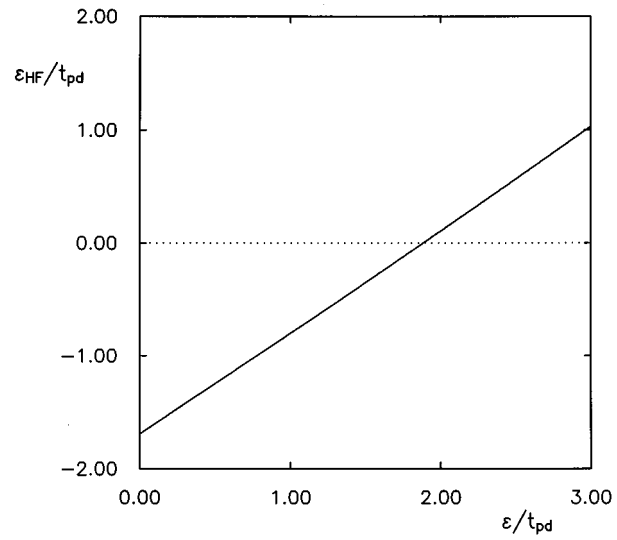

FIG. 21. Variation of the $T\to 0$ Hartree-Fock level separation $\varepsilon_{\rm HF}/t_{pd}$ as a function of the bare level separation ε/t_{pd}. Other parameters are set to their standard values, and $\langle n\rangle = 1.125$.

does the eigenvalue ordering change so that the charge-transfer channel dominates; at such high temperatures neither instability is sufficiently strong to have an important effect.

The first observation with regard to the magnetic eigenvalues in Fig. 19 is that they are always close to unity, dominating the low-temperature physics. The dominant magnetic wave vector is $\mathbf{Q} = (\pi,\pi)$ for all parameters studied with $\langle n\rangle = 1.125$. The eigenvector is in most cases concentrated on the d orbital (basis state 1), and the coefficient of this state increases as ε/t_{pd} is increased.

To understand the effect of ε/t_{pd}, it is useful to monitor the Hartree-Fock level separation

$$\varepsilon_{\rm HF} = \varepsilon + \tfrac{1}{2}U_{pp}\langle n_x\rangle - \tfrac{1}{2}U_{dd}\langle n_d\rangle + 2U_{pd}[\langle n_d\rangle - \langle n_x\rangle - \langle n_y\rangle] \tag{46}$$

as a function of ε; see Fig. 21. For small positive ε the Hartree-Fock level separation is actually negative, indicating that the p levels lie below the d. For larger ε the renormalized level separation becomes positive (the so-called ''charge-transfer regime'' for the high-temperature superconductors[12,25]). As ε continues to increase the system eventually crosses over to a regime completely dominated by the d orbitals which may be described using an effective one-band model[12] (the ''Hubbard regime'').

As an example, for the standard parameter set ($\varepsilon/t_{pd} = 2.75$ and $U_{pd}/t_{pd} = 1$), the dominant magnetic eigenvector has

$$\begin{gathered}\mathbf{Q} = (\pi,\pi),\\ |\langle 1|\phi\rangle|^2 = 0.987,\\ |\langle 2|\phi\rangle|^2 = |\langle 3|\phi\rangle|^2 = 0,\\ |\langle m|\phi\rangle|^2 = 0.002, \quad m = 4,\ldots,11.\end{gathered} \tag{47}$$

[As remarked previously, for $\mathbf{Q} = (\pi,\pi)$, the uncorrelated propagator matrix becomes block-diagonal, and basis state 1

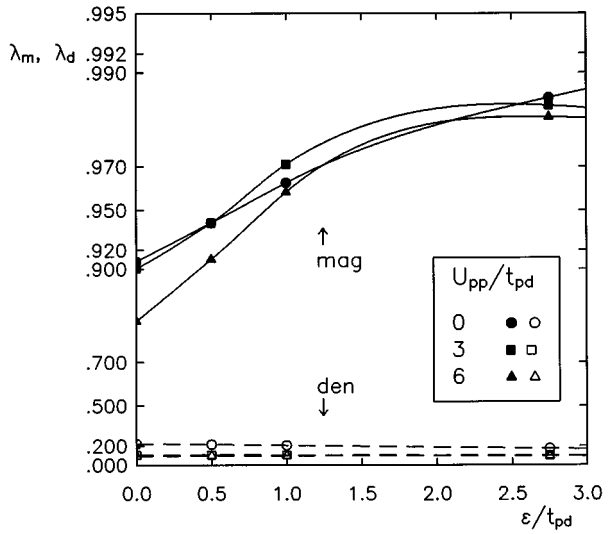

FIG. 22. Maximum magnetic and density channel eigenvalues as a function of bare level separation ε/t_{pd} for three values of U_{pp}/t_{pd}. Other parameters are set at their standard values. The particle density and temperature are as in Fig. 19.

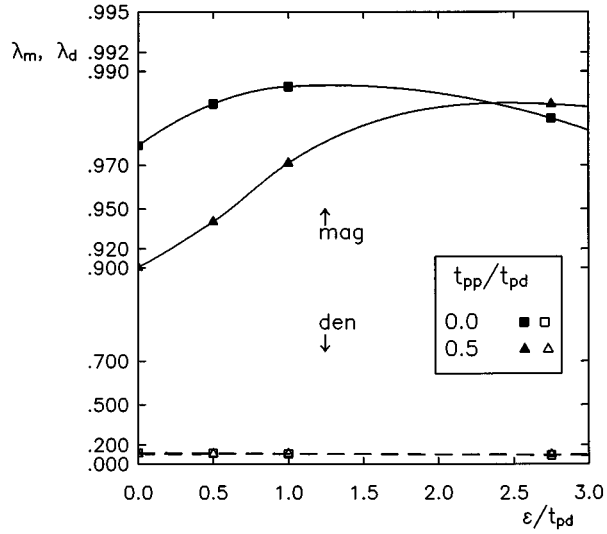

FIG. 23. Maximum magnetic and density channel eigenvalues as a function of bare level separation ε/t_{pd} for two values of t_{pp}/t_{pd}. Other parameters are set at their standard values. The particle density and temperature are as in Fig. 19.

decouples from 2 and 3.] As ε decreases, the admixture of states 2 through 11 grows. Furthermore, for ϵ near 0 and large U_{pd}, the dominant eigenvalue may actually become twofold degenerate (because basis states 2 and 3 take over the role played by 1). For example, for $\varepsilon/t_{pd}=0$ and $U_{pd}/t_{pd}=4$, the magnetic eigenvalue is degenerate, and an eigenvector concentrated on the p_y orbital has

$$\begin{aligned}
&\mathbf{Q}=(\pi,\pi),\\
&|\langle 1|\phi\rangle|^2=0,\\
&|\langle 2|\phi\rangle|^2=0.050,\\
&|\langle 3|\phi\rangle|^2=0.590,\\
&|\langle m|\phi\rangle|^2=0.007, \quad m=4,5,6,7,\\
&|\langle m|\phi\rangle|^2=0.083, \quad m=8,9,10,11.
\end{aligned} \tag{48}$$

Next we consider the role of the Coulomb repulsion on the p_x and p_y orbitals. This matrix element has been neglected in most previous studies, even though it is expected to be the second largest interaction in the model. One expects U_{pp} to suppress the charge-transfer channel, since it increases the energy penalty paid for moving charge from the d to p orbitals. In Fig. 22 we plot λ_m and λ_d versus ε/t_{pd} for $U_{pp}/t_{pd}=0$, 3, and 6, with other parameters in the standard set. The effect on the dominant magnetic channel is slight: The eigenvalue decreases slightly with increasing U_{pp} for large ε, a trend consistent with the suppression of virtual d-p hopping processes by increased repulsion in the p orbitals. The character of the eigenvectors is almost unchanged. For the density channels the effect is somewhat more dramatic, though not evident in the figure. The maximum eigenvalue decreases as expected, but the more important variation appears in the eigenvector. For $U_{pp}/t_{pd}=0$, the dominant channel is the $\mathbf{Q}=\mathbf{0}$ charge transfer; however, when U_{pp}/t_{pd} is increased to 3 (in the standard parameter set) or 6, this channel is suppressed, and the $\mathbf{Q}=\mathbf{0}$ mixed-orbital d-p channel becomes dominant. As an example, for the standard parameter set the density channel eigenvector has

$$\begin{aligned}
&\mathbf{Q}=\mathbf{0},\\
&|\langle m|\phi\rangle|^2=0.125, \quad m=4,\ldots,11,
\end{aligned} \tag{49}$$

with negligible admixture from states 1, 2, and 3. In all cases the dominant density channel is much weaker than the dominant magnetic channel.

While density-functional studies indicate the presence of a p-p transfer matrix element about half as big as the p-d matrix element,[24] most previous model studies have omitted this effect. We examine the effect of t_{pp} in Fig. 23; all other parameters take their standard values. The eigenvalues change only slightly when t_{pp} is turned off. The only qualitative change in the eigenvectors is the shift of the wave vector for the dominant mixed-orbital density channel from $\mathbf{Q}=\mathbf{0}$ to $\mathbf{Q}=(\pi,\pi)$. As noted previously, the wave-vector dependence of this channel is weak, and the shift in the maximum does not represent a significant change in the physics.

Finally we consider in Fig. 24 the effect of variations in U_{dd}, with other parameters fixed at their standard values. As expected, the large-$\mathbf{Q}$ magnetic eigenvalue is suppressed significantly when U_{dd}/t_{pd} is decreased from 8 to 2, but the magnetic channel remains dominant. The reduction of U_{dd} alters the identity of the dominant density channel in the same way noted previously for an increase in U_{pd}: for all values of ϵ in Fig. 24, the dominant density eigenvector is the $\mathbf{Q}=\mathbf{0}$ mixed-orbital state for $U_{dd}/t_{pd}=8$ and the $\mathbf{Q}=\mathbf{0}$ charge-transfer state for $U_{dd}/t_{pd}=2$.

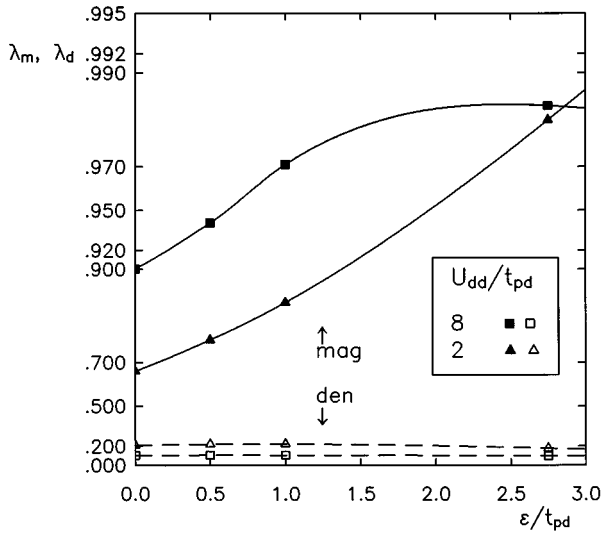

FIG. 24. Maximum magnetic and density channel eigenvalues as a function of bare level separation ε/t_{pd} for two values of U_{dd}/t_{pd}. Other parameters are set at their standard values. The particle density and temperature are as in Fig. 19.

D. Hartree-Fock and FLEX band structure

In this section we analyze the effect of interactions on the one-particle band structure of the CuO_2 model. Within the Hartree-Fock approximation the system may be described by an effective Hamiltonian

$$H^{\mathrm{HF}}-\mu^{\mathrm{HF}}N=\sum_{\sigma}\sum_{ab}\sum_{\mathbf{k}}[h_{ab}^{\mathrm{HF}}(\mathbf{k})-\mu^{\mathrm{HF}}]c_{a\sigma}^{\dagger}(\mathbf{k})c_{b\sigma}(\mathbf{k}),$$
$$h_{ab}^{\mathrm{HF}}(\mathbf{k})=h_{ab}^{0}(\mathbf{k})+\Sigma_{ab}^{(1)}(\mathbf{k}). \tag{50}$$

Both the diagonal and the off-diagonal (i.e., hopping) elements of the Hamiltonian are renormalized. The Hartree-Fock bands are just the eigenvalues of the 3×3 matrix $h^{\mathrm{HF}}(\mathbf{k})-\mu^{\mathrm{HF}}$.

Within the FLEX approximation the self-energy is no longer instantaneous, and quasiparticle bands can only be rigorously defined in the vicinity of the Fermi surface. The FLEX Fermi surface may be determined using the procedure outlined by Luttinger[30] for multiband interacting systems. (This procedure is valid for any conserving approximation and, of course, for the exact model solution.) It is necessary to solve the 3×3 matrix eigenvalue problem

$$\{[h^{0}(\mathbf{k})-\mu^{\mathrm{FLEX}}]+\Sigma(\mathbf{k},\omega=i0^{+})\}\phi_i(\mathbf{k})=\lambda_i(\mathbf{k})\phi_i(k), \tag{51}$$

where the self-energy matrix Σ is evaluated on the *real* axis at the chemical potential ($\omega=0$), $\lambda_i(\mathbf{k})$ is in general a *complex* eigenvalue, and $\phi_i(\mathbf{k})$ is an eigenvector in orbital space. The Fermi surface is the locus of points $\mathbf{k}$ for which

$$\mathrm{Re}\lambda_i(\mathbf{k})=0 \tag{52a}$$

for any of the three eigenvalues. At zero temperature one should also find

$$\mathrm{Im}\lambda_i(\mathbf{k})=0 \tag{52b}$$

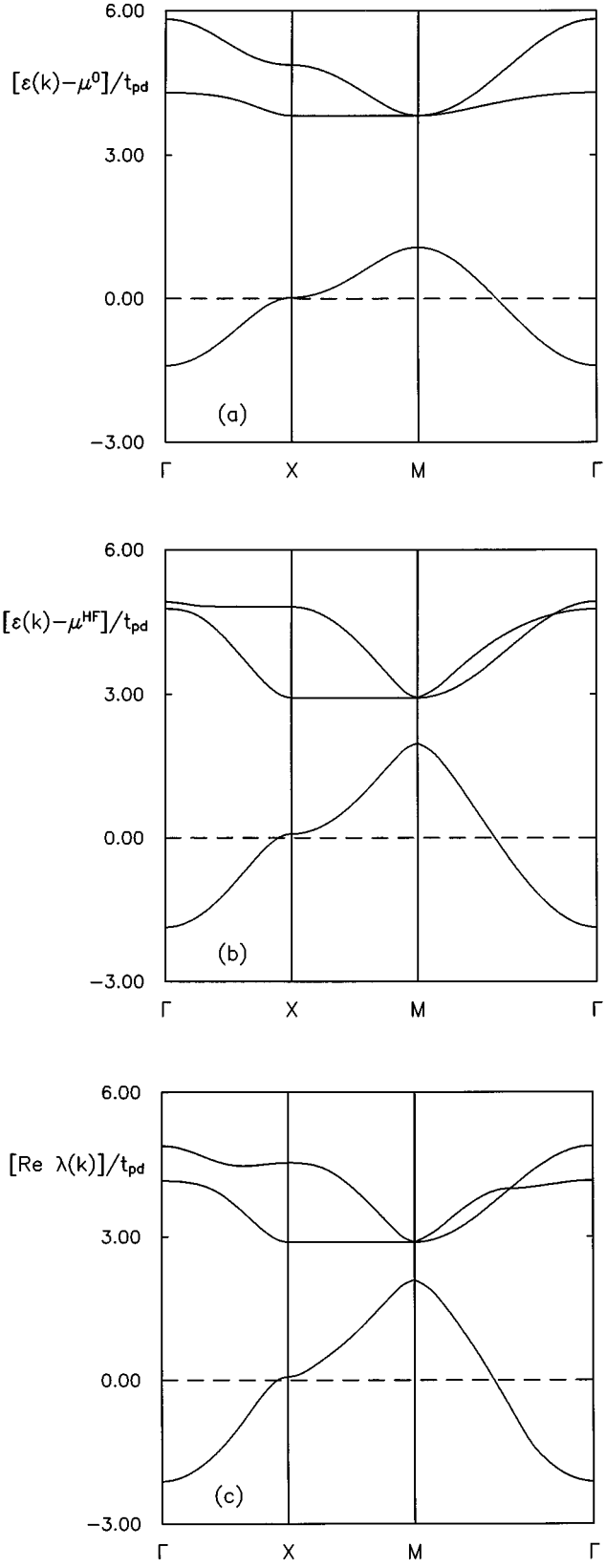

FIG. 25. Dispersion of noninteracting, Hartree-Fock, and FLEX bands along a triangular contour in the Brillouin zone (see Fig. 13). Results are shown for the standard parameter set at $\langle n\rangle=1.125$. The temperature for the FLEX calculation is $T/t_{pd}=0.016$. The chemical potential is indicated by a dashed line. (a) Noninteracting bands. (b) Hartree-Fock bands. (c) FLEX ''bands.'' Note the definition of $\lambda(\mathbf{k})$ in the text.

for points on the Fermi surface; a nonzero imaginary part is expected if the calculation is carried out at finite temperature. According to the so-called Luttinger theorem[30] (whose proof remains valid for any conserving approximation), the volume (or in two-dimensional systems, the area) inside the Fermi surface depends only on the average particle number per unit cell. In other words, Coulomb interactions may distort the Fermi surface from its noninteracting shape, but they do not alter its volume.

In order to study the Luttinger theorem we have performed the analytic continuation of the **k**-dependent self-energy matrix to the real axis using standard Padé approximant techniques.[31] For $\omega\sim 0$ the continuation is highly stable. In fact, the error in determining the Fermi surface using the simple imaginary-axis approximation

$$\Sigma(\mathbf{k},i0^+)\simeq\Sigma(\mathbf{k},i\pi T) \tag{53}$$

is on the order of a few percent for $T/t_{pd}=0.016$.

In the figures which follow we plot the variation of $\mathrm{Re}\lambda_i(\mathbf{k})$ within the Brillouin zone, along with the bands for the noninteracting system, $\varepsilon_i^0(\mathbf{k})-\mu^0$, and the Hartree-Fock system, $\varepsilon_i^{\mathrm{HF}}-\mu^{\mathrm{HF}}$. It is important to note that the FLEX eigenvalues determined in this way should not strictly be interpreted as quasiparticle bands for general **k**. To determine the bands it is necessary to perform the usual procedure of searching for zeros of the inverse propagator using the full frequency-dependent self-energy, not just the value at $\omega=i0^+$. Nevertheless the plots of $\mathrm{Re}\lambda_i(\mathbf{k})$ below furnish at least an approximate global picture of the FLEX band structure, and for brevity we shall refer to them as the ''FLEX bands.''

In Fig. 25 we plot the noninteracting, Hartree-Fock, and FLEX bands along a triangular Brillouin zone contour (see Fig. 13) for the standard parameter set with $\langle n\rangle=1.125$ (hole doping) and a 16×16 discretization. In all cases energies are measured from the appropriate chemical potential. Note that the Brillouin zone labeling is for the choice of checkerboard orbital phases in Fig. 14. For this choice, the hole band minimum occurs at the Γ point. (In contrast, for the uniform phase scheme, the hole band minimum occurs at the M point.)

The band which crosses the Fermi surface has strongly mixed d and p character. For example, for the point at $\mathbf{k}=(7\pi/8,\pi/8)$,

$$\begin{aligned}|\langle d|\phi^{\mathrm{HF}}\rangle|^2&=0.578,\\ |\langle p_x|\phi^{\mathrm{HF}}\rangle|^2&=0.040,\\ |\langle p_y|\phi^{\mathrm{HF}}\rangle|^2&=0.382,\end{aligned} \tag{54}$$

and

$$\begin{aligned}|\langle d|\phi^{\mathrm{FLEX}}\rangle|^2&=0.610,\\ |\langle p_x|\phi^{\mathrm{FLEX}}\rangle|^2&=0.037,\\ |\langle p_y|\phi^{\mathrm{FLEX}}\rangle|^2&=0.353.\end{aligned} \tag{55}$$

Hartree-Fock and FLEX Fermi surfaces (Fig. 26) have been determined for $\langle n\rangle=0.875$ (electron-doped), 1.00 (undoped), and 1.125 (hole-doped) using linear interpolation of the **k**-dependent eigenvalues along a set of one-dimensional trajectories in the discretized Brillouin zone. The FLEX determinations are made at $T/t_{pd}=0.016$ for $\langle n\rangle=0.875$ and 1.125, and at $T/t_{pd}=0.031$ for $\langle n\rangle=1.00$. Only slight deviations from the Luttinger theorem are observed, with the largest discrepancy at $\langle n\rangle=1.00$. These deviations appear to arise entirely from the use of finite temperature FLEX data: the values of $\mathrm{Im}\,\lambda_i(\mathbf{k})$ at the Fermi surface are nonzero and temperature-dependent even at temperatures as low as 0.016. Furthermore, the difference between the FLEX and Hartree-Fock volumes consistently decreases with decreasing temperature. Note that in the Hartree-Fock plots occupied hole states (or equivalently, empty electron states) appear at small **k** (inside the Fermi surface). Note also that if a uniform phase scheme is adopted to label the underlying orbitals, the center point in Figs. 26(a)–26(c) becomes the M point; if the Fermi surface is then replotted in a Brillouin zone centered on Γ, its appearance changes to four disconnected arcs, with occupied hole states centered on the zone corners.

To indicate the effect of t_{pp} on the band structure, we have repeated the calculations described above for $t_{pp}=0$. Results are plotted in Fig. 27 for $\langle n\rangle=1.125$. Two qualitative differences from the full calculation are immediately evident: First, the nearly flat middle band in Fig. 25 becomes a completely dispersionless nonbonding p band. Second and more important, the point at which the Hartree-Fock and FLEX bands cross the Fermi energy moves from the zone interior ($\Gamma\rightarrow X$) to the zone face ($X\rightarrow M$), altering the Fermi surface topology. For our orbital phase scheme (Fig. 14), the Fermi surface becomes four disconnected arcs centered on the M points (still with occupied hole states at small **k**). Conversely, for the uniform phase scheme, it becomes a continuous curve centered on Γ, with occupied hole states outside. This qualitative difference in behavior from the standard parameter set illustrates the crucial role played by t_{pp} in obtaining a valid description of the high-temperature superconductors.

E. Orbital occupancy factors

In this section we discuss the behavior of the orbital occupancy factors

$$n_{ab}(\mathbf{k})=\sum_\sigma\langle c_{b\sigma}^\dagger(\mathbf{k})c_{a\sigma}(\mathbf{k})\rangle=2G_{ab}(\mathbf{k},\tau=0^-). \tag{56}$$

These quantities are just equal-time one-particle propagators. To eliminate numerical cutoff effects, they may be computed as

$$\begin{aligned}n_{ab}(\mathbf{k})=\delta_{ab}&+2T\sum_{|\omega|<\omega_c}G_{ab}(\mathbf{k},i\omega)\\&+\left[n_{ab}^{\mathrm{HF}}(\mathbf{k})-\delta_{ab}-2T\sum_{|\omega|<\omega_c}G_{ab}^{\mathrm{HF}}(\mathbf{k},i\omega)\right],\end{aligned} \tag{57}$$

where the Hartree-Fock corrections are evaluated using the FLEX chemical potential and $\Sigma^{(1)}$.

The diagonal occupancy factors $n_{dd}(\mathbf{k})$, $n_{xx}(\mathbf{k})$, and $n_{yy}(\mathbf{k})$ are plotted for the standard parameter set with $\langle n\rangle=1.125$ (hole doping) and $T/t_{pd}=0.016$ in Fig. 28. (Note that the occupancy factors count the average number of

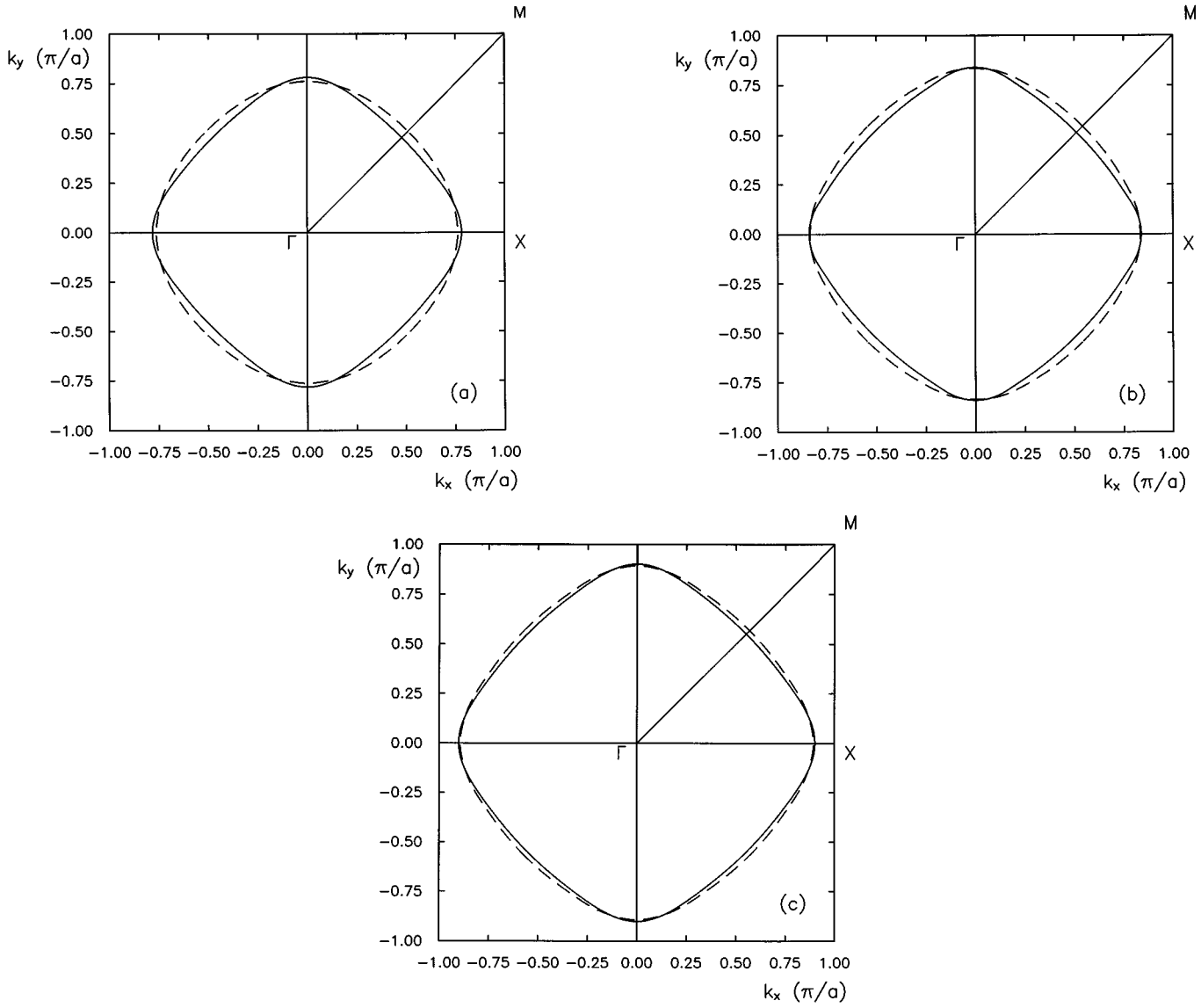

FIG. 26. Comparison of Hartree-Fock and FLEX Fermi surfaces for a range of particle densities. The FLEX results are calculated at $T/t_{pd}=0.016$ for (a) and (c), and at $T/t_{pd}=0.031$ for (b). A dashed line indicates the Hartree-Fock surface, and a solid line the FLEX surface. (a) $\langle n\rangle=0.875$ (electron doping). (b) $\langle n\rangle=1.00$ (undoped). (c) $\langle n\rangle=1.125$ (hole doping).

holes, not electrons.) Results from Hartree-Fock and full FLEX calculations are shown. Points at which $\mathbf{k}$ crosses the Fermi surface are indicated by arrows. Note that for $\mathbf{k}$ along the zone edge, i.e., $\mathbf{k}=(\pi,k_y)$, the FLEX occupancy factor $n_{xx}(\mathbf{k})$ drops nearly to zero. This is because the Fermi surface band has no p_x hybridization for these values of $\mathbf{k}$. Note also that, as mentioned previously, states at the Fermi surface have strong admixtures of both the d and p orbitals.

The FLEX occupancy factors do not exhibit sharp discontinuities at the Fermi surface for the range of temperatures studied here. Discontinuities proportional to the wave-function renormalization constant $Z_{\mathbf{k}}$ are expected within Fermi liquid theory for $T\rightarrow 0$. While Fermi liquid behavior is evident in the Hartree-Fock results, the FLEX results exhibit only a Fermi surface crossover region, whose width is controlled by strong residual scattering for temperatures as low as $T/t_{pd}=0.016$. The present study does not allow a prediction of normal state behavior in the asymptotic zero-temperature limit; however, if Fermi liquid behavior is attained, the relevant temperature scale must be much less than $T/t_{pd}=0.016$. In any case, it is likely that a superconducting transition preempts the attainment of this limit, at least within FLEX.

It is of interest to compare the results in Fig. 28 with results for a simplified CuO_2 model with $U_{pp}=U_{pd}=0$, and t_{pd}, t_{pp}, ϵ, and U_{dd} fixed at their standard values. The simplified model results (Fig. 29) are, as expected, extremely similar. Gross details of the Fermi surface and the degree of hybridization are largely determined by the form of the one-particle Hamiltonian. The most obvious difference brought about by turning on U_{pp} and U_{pd} is a slight decrease in $n_{xx}(\mathbf{k})$ and $n_{yy}(\mathbf{k})$ due to an increased energy penalty for occupancy of the p orbitals. The total FLEX occupancy per unit cell for either the p_x or p_y orbital drops from 0.22 to 0.19 when U_{pp} and U_{pd} are increased from zero to their standard values.

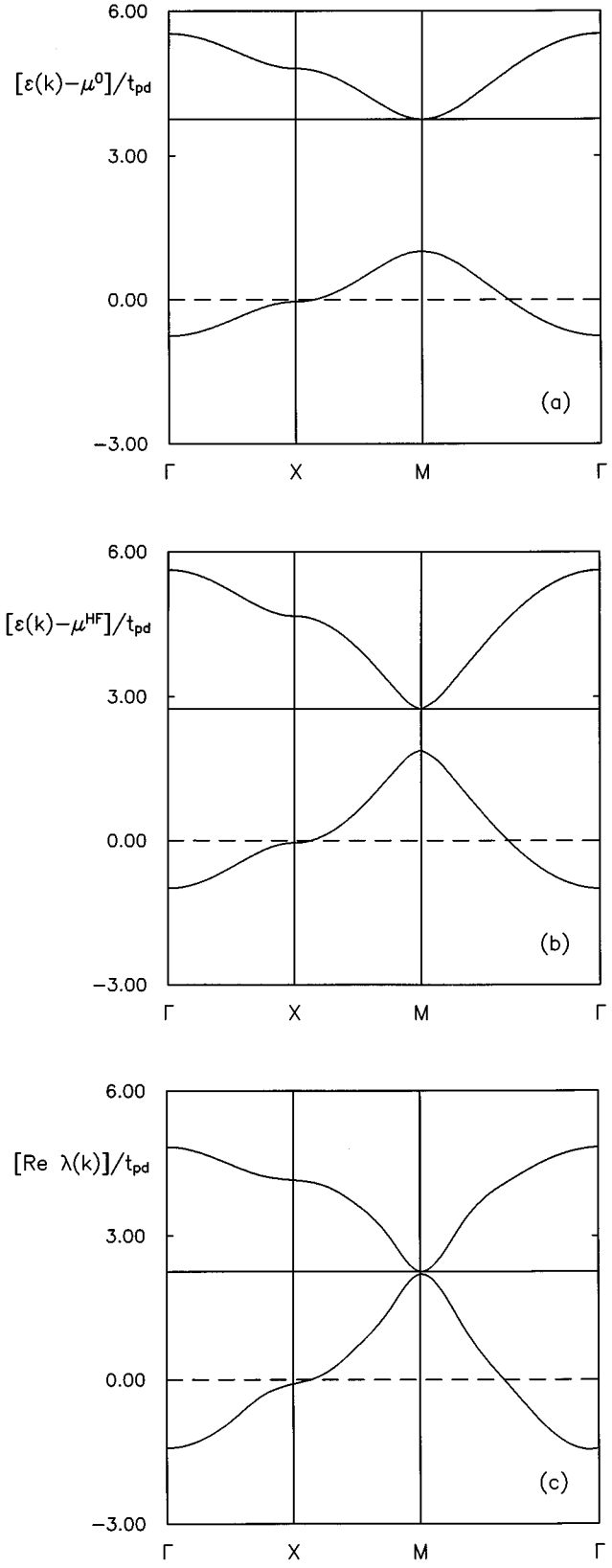

FIG. 27. Dispersion of noninteracting, Hartree-Fock, and FLEX bands for $t_{pp}=0$ and other parameters at their standard values. The density is $\langle n\rangle=1.125$ (hole doping). (a) Noninteracting bands. (b) Hartree-Fock bands. (c) FLEX ''bands.'' We attach no particular significance to the closing of the FLEX band gap at the M point: Recall that the eigenvalues $\mathrm{Re}\lambda_i(\mathbf{k})$ are calculated with the $\omega=0$ self-energy matrix (see text).

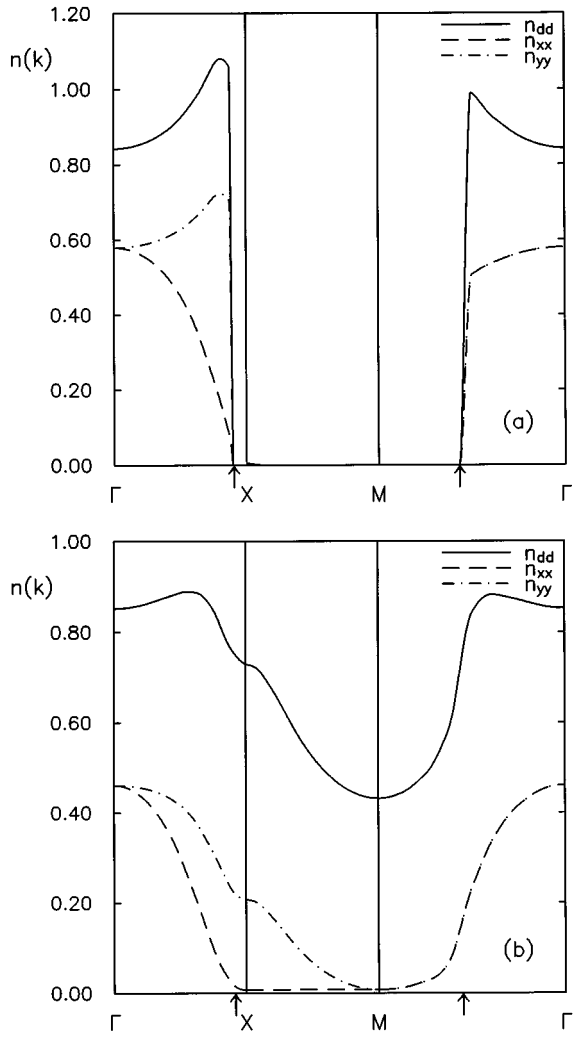

FIG. 28. Variation of the diagonal elements of the orbital-projected occupancy factor $n(\mathbf{k})$ along the triangular Brillouin zone contour. The points at which $\mathbf{k}$ crosses the Fermi surface are indicated by arrows. Parameters take on their standard values, with $\langle n\rangle=1.125$ (hole doping) and $T/t_{pd}=0.016$. (a) Hartree-Fock result. (b) FLEX result. Note that the FLEX occupancy factors remain large outside the Fermi surface, where the Hartree-Fock occupancy drops to zero.

F. One-particle spectral densities

The orbital-projected one-particle spectral density ρ_{ab} is just the real-axis discontinuity in the propagator matrix:

$$\rho_{ab}(\mathbf{k},\omega)=-\frac{1}{2\pi i}\left[G_{ab}(\mathbf{k},\omega+i0^{+})-G_{ab}(\mathbf{k},\omega+i0^{-})\right]. \tag{58}$$

It is straightforward to show, using fermion anticommutation relations, that ρ_{ab} satisfies the sum rule

$$\int_{-\infty}^{\infty} d\omega\ \rho_{ab}(\mathbf{k},\omega)=\delta_{ab}\,. \tag{59}$$

The diagonal elements of the spectral density are positive definite and have a simple physical interpretation. The spectral weight for removing a particle from the system with

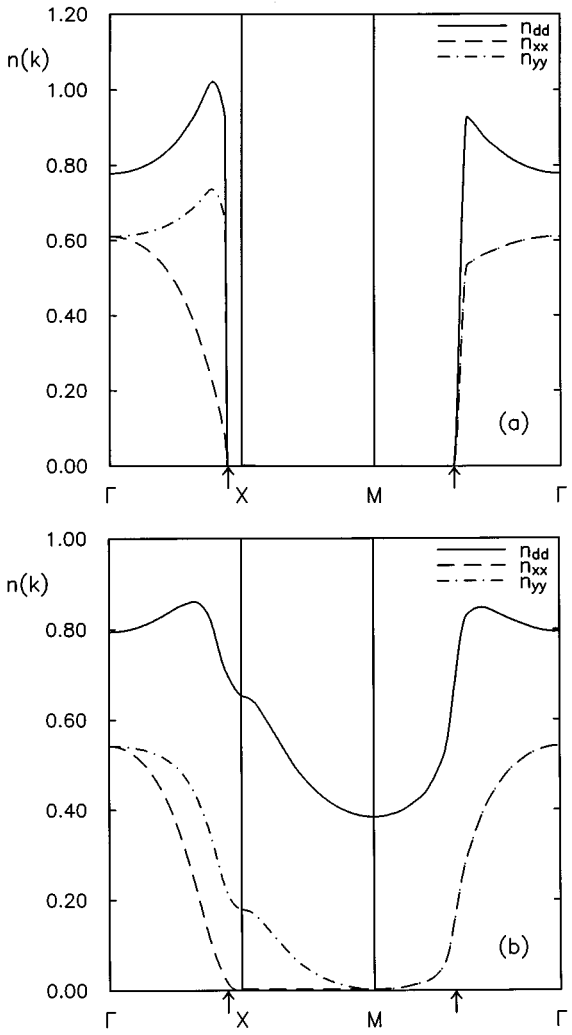

FIG. 29. Variation of the diagonal elements of the orbital-projected occupancy factor $n(\mathbf{k})$ along the triangular Brillouin zone contour. In this case $U_{pp}=U_{pd}=0$, while other parameters are as in Fig. 28. As before, arrows indicate the position of the Fermi surface. (a) Hartree-Fock result. (b) FLEX result.

wave vector $\mathbf{k}$ and energy ω in orbital a is just $f(\omega)\rho_{aa}(\mathbf{k},\omega)$, with f the Fermi function

$$f(\omega)=(e^{\beta\omega}+1)^{-1}. \tag{60}$$

Conversely, the spectral weight for adding a particle to the system with the same characteristics is $[1-f(\omega)]\rho_{aa}(\mathbf{k},\omega)$. Since the diagonal elements are real, Eq. (58) may be simplified as

$$\rho_{aa}(\mathbf{k},\omega)=-\frac{1}{\pi}\,\mathrm{Im}G_{aa}(\mathbf{k},\omega+i0^{+}). \tag{61}$$

The off-diagonal elements of the spectral density are not positive definite and may even be complex. These elements describe the process of adding a particle to the system in one orbital and removing it in another. Their calculation is straightforward, but in the discussion which follows we restrict attention to the diagonal elements.

The functions $\rho_{aa}(\mathbf{k},\omega)$ may be obtained from our imaginary-axis propagator data by numerical analytic continuation. Several techniques are available for this purpose, including the maximum-entropy data reconstruction technique,[32,33] which has become standard in quantum Monte Carlo studies. In this paper we use instead the Padé, or rational function, approximant technique.[31] Padé approximants allow convenient consistency checks on the quality of imaginary-axis data, since they do *not* impose *a priori* constraints based on positivity and sum rules. Checks on the spectral densities include (i) positivity, (ii) overall normalization [Eq. (59)], and (iii) normalization of occupied states, i.e.,

$$2\int_{-\infty}^{\infty}d\omega\; f(\omega)\rho_{ab}(\mathbf{k},\omega)=n_{ab}(\mathbf{k}). \tag{62}$$

For the results shown below the sum rules in Eqs. (59) and (62) hold true at better than 1%.

We limit our discussion to the standard parameter set. Results for the simplified ($U_{pp}=U_{pd}=0$) parameters set discussed in Sec. IV E are quantitatively very similar. Results are plotted for $\langle n\rangle=1.125$ (hole doping) and a 16×16 $\mathbf{k}$-space discretization. Note that the required analytic continuation may be performed on either the self-energy matrix $\Sigma_{ab}(\mathbf{k},i\omega)$ or the propagator $G_{ab}(\mathbf{k},i\omega)$. We have found it more numerically stable to continue the propagator.

A series of temperature-dependent plots of the d-orbital density $\rho_{dd}(\mathbf{k},\omega)$ are shown in Fig. 30(a) for $\mathbf{k}=(7\pi/8,\pi/8)$, a point very close to the FLEX Fermi surface. A closeup view of the low-energy behavior is included as Fig. 30(b). The spectral density within the Hartree-Fock approximation for $T\rightarrow0$ (a set of three δ functions) is shown for comparison in Fig. 30(a). The weight of the Hartree-Fock δ functions indicates the degree of admixture of the d orbital in the three band states at this value of $\mathbf{k}$. Since k_x is close to π, the d orbital mixes only weakly with the p_x orbital, but strongly with the p_y orbital. The low-intensity δ function at $\omega/t_{pd}\sim3$ locates the ''nonbonding'' band state (almost entirely p_x in parentage), while the higher-intensity δ functions at $\omega/t_{pd}\sim0$ and 5 locate the ''bonding'' and ''antibonding'' states (strong admixtures of d and p_y, with only a slight admixture of p_x). The FLEX spectral densities may be described qualitatively as follows: The Hartree-Fock δ functions are smeared into resonances of finite width, which shift slightly and narrow with decreasing temperature. The structure near the Fermi surface [Fig. 30(b)] is strongly temperature dependent, due to the effect of low-energy spin fluctuations. A prominent quasiparticle peak develops from the Fermi surface band as the temperature is decreased.

Analogous plots for $\rho_{xx}(\mathbf{k},\omega)$ and $\rho_{yy}(\mathbf{k},\omega)$ are shown in Figs. 31 and 32. The features can again be understood as a modification of the Hartree-Fock results. Note that ρ_{xx} is dominated by a broad resonance at $\omega/t_{pd}\sim3$, the remnant of the Hartree-Fock ''nonbonding'' state. The presence of a small admixture of the p_x orbital in the Hartree-Fock band state at $\omega\sim0$ accounts for the Fermi surface peak in ρ_{xx}. Note that although the integrated weight in this peak is small in comparison with that in ρ_{dd}, the temperature dependence is quite similar [Fig. 31(b)]. The ρ_{yy} density is a superposition of two strong peaks, which correspond to the ''bonding'' and ''antibonding'' Hartree-Fock band states. The temperature dependence of the Fermi surface peak again mirrors the behavior in ρ_{dd}.

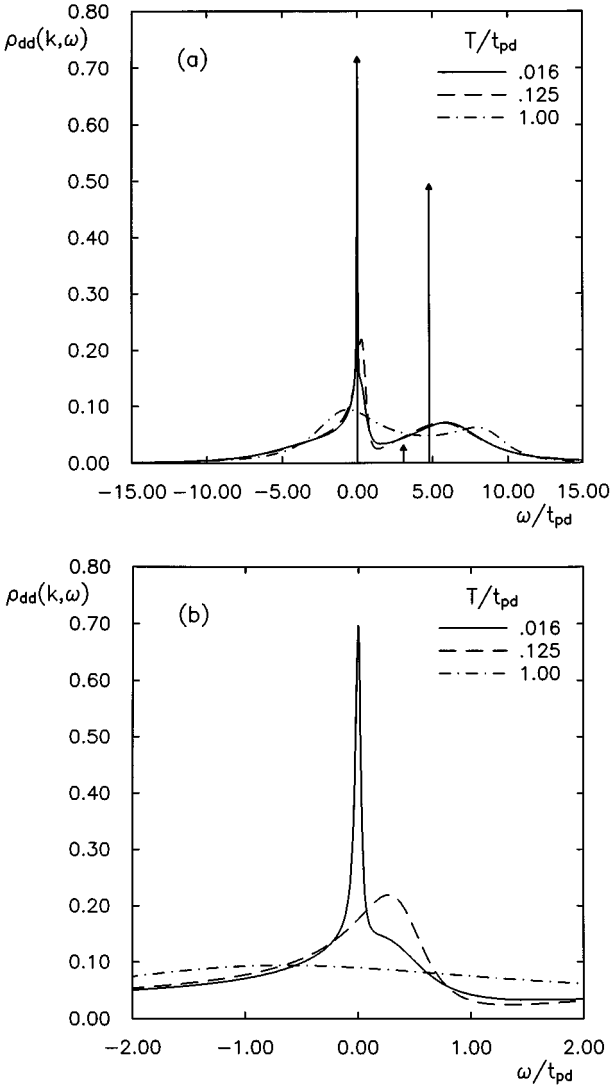

FIG. 30. Temperature variation of the d-orbital spectral density $\rho_{dd}(\mathbf{k},\omega)$. Parameters take on their standard values, with $\langle n\rangle = 1.125$ (hole doping). The wave vector is $\mathbf{k}=(7\pi/8,\ \pi/8)$, a point as close as possible to the Fermi surface for a 16×16 discretization. Vertical arrows indicate the positions and relative weights for the three δ functions contributing to ρ_{dd} in a $T\rightarrow0$ Hartree-Fock calculation. The FLEX spectral densities are positive-definite and integrate to unity at the 1% level. (a) Full-scale variation of ρ_{dd}. (b) Fine-scale variation near the Fermi energy.

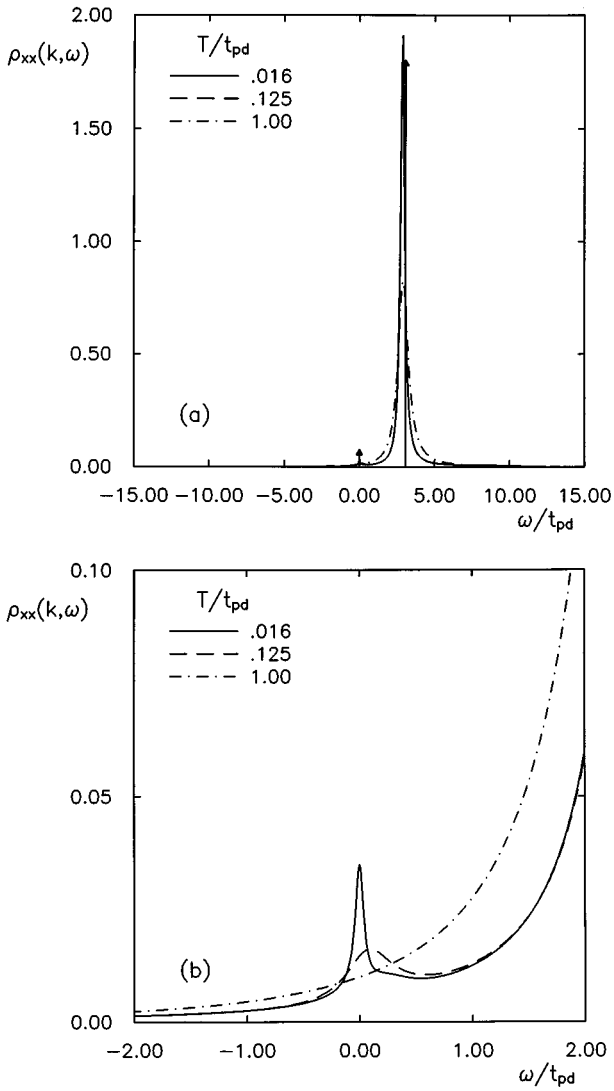

FIG. 31. Temperature variation of the p_x-orbital spectral density $\rho_{xx}(\mathbf{k},\omega)$. Parameters are as in Fig. 30. As before, vertical arrows indicate the Hartree-Fock δ functions. (a) Full-scale variation of ρ_{xx}. (b) Fine-scale variation near the Fermi energy.

G. Spectral densities for particle-hole fluctuations

Even though vertex-corrected dynamic susceptibilities are not determined in this paper, it is of interest to examine the spectral densities for the correlated fluctuation propagators M and D. In analogy with the one-particle spectral densities, we write

$$\sigma_{ij}(\mathbf{Q},\omega)=\frac{1}{2\pi i}\,[M_{ij}(\mathbf{Q},\omega+i0^{+})-M_{ij}(\mathbf{Q},\omega+i0^{-})], \tag{63}$$

where M is the correlated spin fluctuation propagator, and i and j run over the 11 particle-hole basis states in Table I. As before, the interpretation of diagonal elements of the spectral density matrix is simplest. It is straightforward to show that $\sigma_{ii}(\mathbf{Q},\omega)$ is real-valued so that Eq. (63) may be simplified as

$$\sigma_{ii}(\mathbf{Q},\omega)=\frac{1}{\pi}\,\mathrm{Im}M_{ii}(\mathbf{Q},\omega+io^{+}). \tag{64}$$

Furthermore, it follows that

$$\sigma_{ij}(\mathbf{Q},0)=0 \tag{65a}$$

and

$$(\mathrm{sgn}\omega)\sigma_{ii}(\mathbf{Q},\omega)>0. \tag{65b}$$

Finally, the spectral density satisfies the symmetry relation

$$\sigma_{ii}(\mathbf{Q},\omega)=-\sigma_{\bar{i}\bar{i}}(-\mathbf{Q},-\omega), \tag{66}$$

for states i and $\bar{i}$ related by particle-hole conjugation. For example, the particle-hole conjugate of state 5 (d particle one site to the right of p_x hole) is state 7 (p_x particle one site to the left of d hole). It is *not* true in general that σ_{ii} is an odd

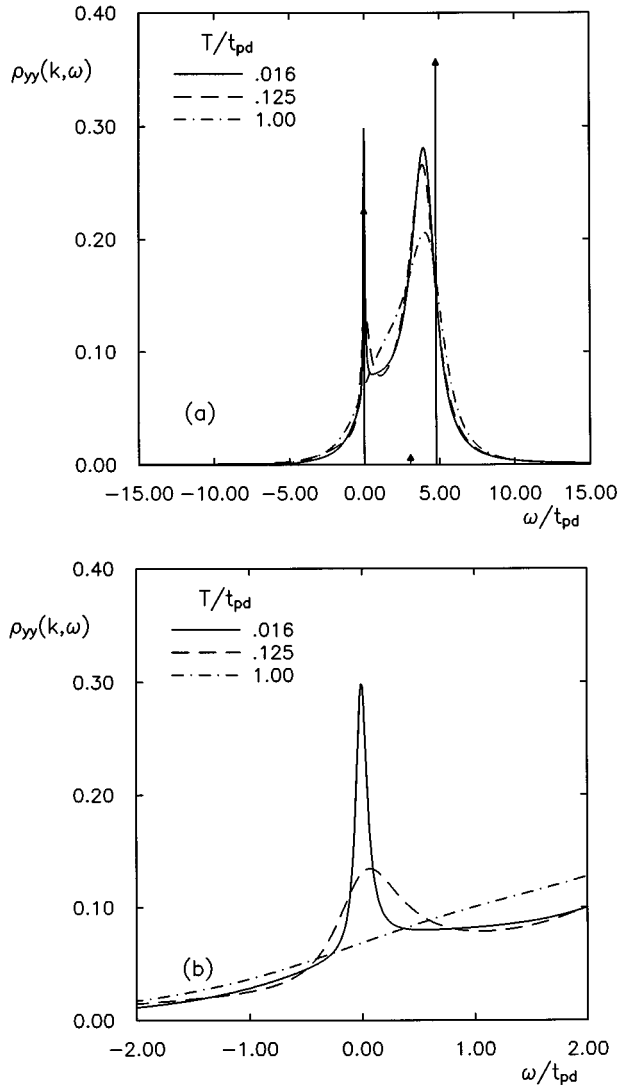

FIG. 32. Temperature variation of the p_y-orbital spectral density $\rho_{yy}(\mathbf{k},\omega)$. Parameters are as in Fig. 30. As before, vertical arrows indicate the Hartree-Fock δ functions. (a) Full-scale variation of ρ_{yy}. (b) Fine-scale variation near the Fermi energy.

function of ω, as one might expect by analogy with single-orbital models. It follows, however, from Eq. (66) and inversion symmetry that

$$\sigma_{ii}(\mathbf{Q},\omega) = -\sigma_{ii}(\mathbf{Q},-\omega) \quad \text{if } i=\overline{\imath}, \tag{67}$$

i.e., for $i=1$, 2, or 3 in the CuO_2 model (see Table I).

The diagonal density elements have the following physical interpretation: The spectral weight for removing a spin fluctuation (i.e., an $S=1$ particle-hole pair) from the system with wave vector $\mathbf{Q}$ and energy ω in orbital-pair state i, *or* adding a spin fluctuation to the system with wave vector $-\mathbf{Q}$ and energy $-\omega$ in orbital-pair state $\overline{\imath}$ is just $b(\omega)\sigma_{ii}(\mathbf{Q},\omega)$, with b the Bose function

$$b(\omega) = (e^{\beta\omega}-1)^{-1}. \tag{68}$$

If one interchanges the processes of removal and addition, the corresponding spectral weight is $[1+b(\omega)]\sigma_{ii}(\mathbf{Q},\omega)$. Clearly the latter process for parameters $\mathbf{Q}\to-\mathbf{Q}$, $\omega\to-\omega$, and $i\to\overline{\imath}$ is identical with the former, so that necessarily

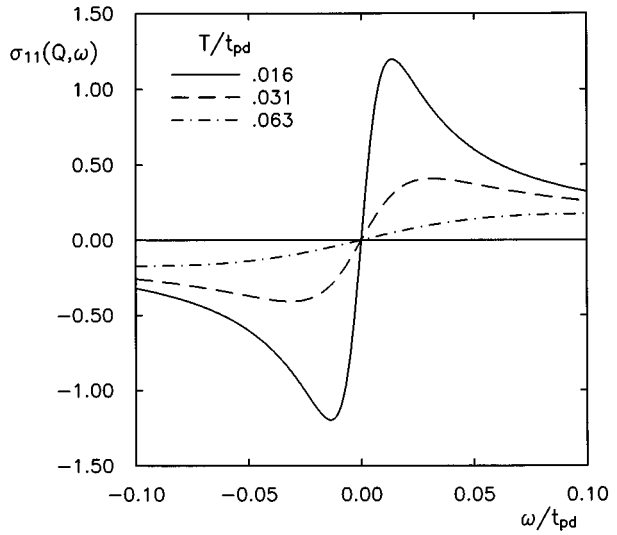

FIG. 33. Temperature variation of the spectral weight $\sigma_{11}(\mathbf{Q},\omega)$ for the d-orbital-projected magnetic propagator. The wave vector $\mathbf{Q}=(\pi,\pi)$, and other parameters are as in Fig. 30. Note that this spectral weight matrix element is odd in frequency.

$$b(\omega)\sigma_{ii}(\mathbf{Q},\omega) = [1+b(-\omega)]\sigma_{\overline{ii}}(-\mathbf{Q},-\omega). \tag{69}$$

The last equation is just a restatement of the symmetry relation in Eq. (66).

We have analytically continued the magnetic particle-hole propagator $M_{ii}(\mathbf{Q},i\Omega)$ to the real axis, again using the Padé approximant technique. As an example, the magnetic d-d spectral density (σ_{11}) is plotted in Fig. 33 for a series of decreasing temperatures with the standard parameter set and $\langle n\rangle = 1.125$ (hole doping). The lattice discretization is 8×8, and the wave vector $\mathbf{Q}$ is (π,π). This spectral density is odd in frequency, in agreement with Eq. (67). Note that a strong low-frequency peak develops as the temperature is reduced. This peak indicates an accumulation of low-lying states in the system with spin 1 and wave vector (π,π). The presence of such states is implied by the rapid increase in the static component of the magnetic propagator at low temperature (see Sec. IV C). If an actual magnetic instability occurred, the resulting ordered state could be viewed as a condensate of particle-hole pairs in these low-energy states.

To illustrate the behavior of $\sigma_{ii}(\mathbf{Q},\omega)$ for i describing an interorbital particle-hole pair, results for $\sigma_{55}(\mathbf{Q},\omega)$ and $\sigma_{77}(-\mathbf{Q},\omega)$ are plotted in Fig. 34(a). As before, the wave vector is $\mathbf{Q}=(\pi,\pi)$. Note that neither function is odd in frequency, but that the two functions satisfy the symmetry relation in Eq. (66). Finally, it is interesting to note [Fig. 34(b)] that because states 5 and 7 have a small, but nonzero, admixture in the unstable (π,π) magnetic eigenvector (see Sec. IV C), they show the same temperature-dependent low-frequency behavior as σ_{11}. Note that, as expected, the integrated spectral weight is much smaller in this case.

V. SUMMARY

Our results may be summarized first with respect to the CuO_2 model studied in Sec. IV, then with respect to general lattice models. Our primary conclusion for the CuO_2 model with unit-cell occupancy close to unity (hole doping or elec-

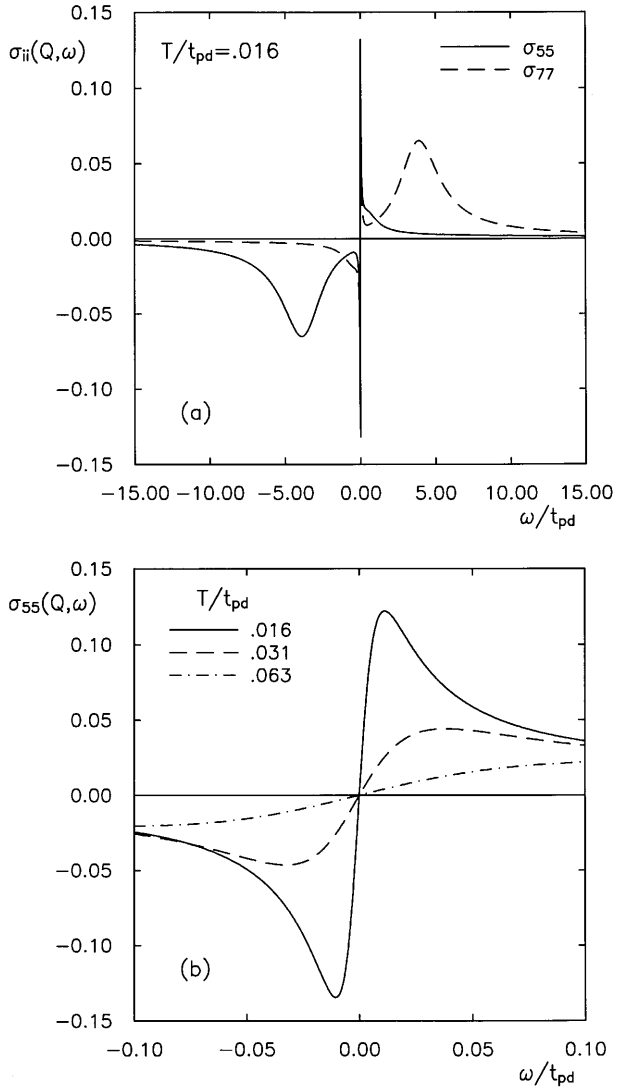

FIG. 34. Comparison of spectral densities $\sigma_{55}(\mathbf{Q},\omega)$ and $\sigma_{77}(-\mathbf{Q},\omega)$ for interorbital magnetic fluctuations. Parameters are as in Fig. 33. Note that in this case the wave vectors $\mathbf{Q}=(\pi,\pi)$ and $-\mathbf{Q}=(-\pi,-\pi)$ describe the same point in the Brillouin zone. (a) Full-scale variation at temperature $T/t_{pd}=0.016$. (b) Fine-scale variation of σ_{55} as a function of temperature.

tron doping) is that the only incipient particle-hole instability is in a spin-1 (i.e., magnetic) channel with $\mathbf{Q}\sim(\pi,\pi)$. The spin-0, or density, channel is never close to an instability for realistic values of the Coulomb integrals. Depending on the values of U_{dd}, U_{pp}, and U_{pd}, the most unstable density channel corresponds either to charge-transfer fluctuations of the type discussed in Refs. 18–20 and 25 or to mixed-orbital fluctuations mediated by the exchange part of the near-neighbor Coulomb interaction. For the standard parameter set of Ref. 24 we find that the mixed-orbital fluctuations are actually dominant.

The Luttinger theorem[30] has been examined and validated for a nontrivial three-band model within the limitations imposed by an analysis for nonzero, but low, temperature. Despite the striking difference between the orbital-projected occupancy factors (Figs. 28 and 29) calculated within the Hartree-Fock and FLEX approximations, the area enclosed by the Fermi surface (or curve, in this case) is preserved, with the shape distorted only slightly.

The results obtained for spectral densities of the one-particle and particle-hole propagators are influenced by the development of low-frequency, large-**Q** spin fluctuations. It is interesting to note in passing the similarity of these results to those for the local orbital in an Anderson impurity model. In both cases the physics is dominated by an incipient magnetic instability, with the resulting development of low-frequency peaks in the spectral densities. This similarity has been previously emphasized in studies of the Hubbard model in the limit of infinite spatial dimension.[34]

An obvious next step in the analysis of the CuO_2 model is the study of instabilities in the particle-particle channel. It is clear from the form of the correlated particle-hole propagators that a singlet channel with $d_{x^2-y^2}$ symmetry will be enhanced, just as in previous studies of the single-orbital Hubbard model[2,6–10] and in apparent agreement with experiments on the cuprate high-temperature superconductors.[35] A direct determination of the superconducting phase diagram (with a quantitative estimate of transition temperatures, albeit within the limitations of the FLEX approximation) is desirable. Such a determination will yield values for the relative weight of the Cooper pair wave function on copper and oxygen sites, with near-neighbor Cu-O Coulomb repulsion taken into account.

In a more general context, the results obtained here provide an encouraging step in the approximate treatment of multiband interacting systems. The FLEX approximation provides a rather natural starting point for the analysis of any system in which particle-hole correlations are appreciable, i.e., narrow-band systems with large Coulomb integrals. The primary limitation of FLEX is its inherent inconsistency in the treatment of two-body vertex functions. One approach to address this limitation is the introduction of self-consistently determined instantaneous pseudopotentials.[3,16] The use of limited particle-hole basis sets indexed by relative separation, rather than relative momentum, provides a potentially crucial tool[21] for going beyond pseudopotentials to the determination of crossing-symmetric self-consistent vertex functions.

Finally, it is important to note that parallel computers provide a natural route for obtaining the time and storage capabilities necessary to treat much more realistic tight-binding models with complex unit-cell structure and longer-range Coulomb interactions. Parallel FLEX implementations have already been obtained for single-orbital models with pure Coulomb[4] and Coulomb+(local phonon)[36] interactions. The independent computation of large numbers of self-energy and particle-hole propagator matrix elements, which is the time-consuming step in a multiband FLEX solution, is well-suited to implementation on a parallel machine, and it is likely that future analyses will be performed in this way.

ACKNOWLEDGMENT

This work was supported in part by the National Science Foundation under Grant No. DMR-9520636.

[1] For a technical introduction see, e.g., N. E. Bickers and D. J. Scalapino, Ann. Phys. (N.Y.) **193**, 206 (1989).
[2] N. E. Bickers, D. J. Scalapino, and S. R. White, Phys. Rev. Lett. **62**, 961 (1989).
[3] N. E. Bickers and S. R. White, Phys. Rev. B **43**, 8044 (1991).
[4] J. W. Serene and D. W. Hess, Phys. Rev. B **44**, 3391 (1991).
[5] C.-H. Pao and N. E. Bickers, Phys. Rev. B **49**, 1586 (1994).
[6] C.-H. Pao and N. E. Bickers, Phys. Rev. Lett. **72**, 1870 (1994).
[7] P. Monthoux and D. J. Scalapino, Phys. Rev. Lett. **72**, 1874 (1994).
[8] St. Lenck, J. P. Carbotte, and R. C. Dynes, Phys. Rev. B **50**, 10 149 (1994).
[9] T. Dahm and L. Tewordt, Phys. Rev. Lett. **74**, 793 (1995).
[10] C.-H. Pao and N. E. Bickers, Phys. Rev. B **51**, 16 310 (1995).
[11] J. Luo and N. E. Bickers, Phys. Rev. B **47**, 12 153 (1993).
[12] V. J. Emery, Phys. Rev. Lett. **58**, 2794 (1987).
[13] A fluctuation exchange, or t-matrix, approximation for the homogeneous electron gas was written down by Baym and Kadanoff in their seminal work on SCF theories: G. Baym and L. P. Kadanoff, Phys. Rev. **124**, 287 (1961); G. Baym, *ibid*. **127**, 1391 (1962).
[14] A. B. Migdal, Zh. Eksp. Teor. Fiz. **34**, 1438 (1958) [Sov. Phys. JETP **7**, 996 (1958)].
[15] G. M. Eliashberg, Zh. Eksp. Teor. Fiz. **38**, 966 (1960) [Sov. Phys. JETP **11**, 696 (1960)].
[16] J. Luo and N. E. Bickers, Phys. Rev. B **48**, 15 983 (1993).
[17] Relative separation basis sets for particle-hole excitations were first introduced in the context of semiconductor theory. See, e.g., W. R. Hanke and L. J. Sham, Phys. Rev. B **12**, 4501 (1975).
[18] P. B. Littlewood, C. M. Varma, S. Schmitt-Rink, and E. Abrahams, Phys. Rev. B **39**, 12 371 (1989).
[19] Y. Bang, K. Quader, E. Abrahams, and P. B. Littlewood, Phys. Rev. B **42**, 4865 (1990).
[20] Y. Bang, G. Kotliar, R. Raimondi, C. Castellani, and M. Grilli, Phys. Rev. B **47**, 3323 (1993).
[21] N. E. Bickers and G. Esirgen (unpublished).
[22] The checkerboard phase pattern is convenient because the resulting one-particle orbitals have a simple $d_{x^2-y^2}$ rotational symmetry about a general Cu site. For this reason, the overall symmetry of particle-hole and particle-particle *pair* states can be displayed explicitly as a ''pair phase,'' rather than implicitly as a combination of phases for the pair and its one-particle components. (This means that the p and d character of the one-particle orbitals can be effectively hidden in the analysis of possible superconducting states.) See also the discussion of symmetries in Sec. III.
[23] Note that the fluctuation spectral densities in Sec. IV G should not be strictly interpreted as dynamic susceptibilities since they are calculated with unrenormalized particle-hole interactions, rather than with full particle-hole vertex functions.
[24] M. S. Hybertsen, M. Schlüter, and N. E. Christensen, Phys. Rev. B **39**, 9028 (1989). Similar values for the tight-binding parameters have been obtained by other groups. See, e.g., A. K. McMahan, R. M. Martin, and S. Satpathy, Phys. Rev. B **38**, 6650 (1988), and E. B. Stechel and D. R. Jennison, *ibid*. **38**, 4632 (1988).
[25] C. M. Varma, S. Schmitt-Rink, and E. Abrahams, Solid State Commun. **62**, 681 (1987).
[26] V. J. Emery and G. Reiter, Phys. Rev. B **38**, 4547 (1988).
[27] J. E. Hirsch, S. Tang, E. Loh, and D. J. Scalapino, Phys. Rev. Lett. **60**, 1668 (1988); Phys. Rev. B **39**, 243 (1989).
[28] R. T. Scalettar, D. J. Scalapino, R. L. Sugar, and S. R. White, Phys. Rev. B **44**, 770 (1991).
[29] G. Dopf, A. Muramatsu, and W. Hanke, Phys. Rev. Lett. **68**, 353 (1992).
[30] J. M. Luttinger and J. C. Ward, Phys. Rev. **118**, 1417 (1960); J. M. Luttinger, *ibid*. **119**, 1153 (1960).
[31] See, e.g., H. J. Vidberg and J. W. Serene, J. Low Temp. Phys. **29**, 179 (1977).
[32] M. Jarrell and O. Biham, Phys. Rev. Lett. **63**, 2504 (1989).
[33] R. N. Silver, D. S. Sivia, and J. E. Gubernatis, Phys. Rev. B **41**, 2380 (1990).
[34] See, e.g., M. J. Rozenberg, X. Y. Zhang, and G. Kotliar, Phys. Rev. Lett. **69**, 1236 (1992); A. Georges and W. Krauth, *ibid*. **69**, 1240 (1992).
[35] See, e.g., the experimental reports cited in Refs. 6, 7, and 9.
[36] C.-H. Pao and H.-B. Schüttler (private communication).